



University of Crete
Physics Department



FO.R.T.H
Institute of Electronic
Structure and Laser

Terahertz spectroscopy of macromolecular systems

Christina Daskalaki

Thesis
For the degree of Master of Science

Heraklion
October 2012

Acknowledgments

I would like to take the opportunity to thank all the people that supported me during my Master of Science at the Physics Department of the University of Crete and helped me to successfully complete the work presented in this thesis.

First of all, I would like to express my gratitude to my supervisor Prof. Stelios Tzortzakis for giving me the opportunity to work in the UNIS group in the Institute of Electronic Structure and Lasers in FORTH. His guidance and support he provided at all levels during this year of my master studies was really important for me.

I would also like to thank Prof. Kostas Fotakis and Prof. Dimitris Papazoglou for being in my master thesis committee.

Furthermore I would like to especially thank Maria Massaouti for her help and support inside the lab and her guidance in my experimental work. Thanks to her effort and patience, I gained knowledge that helped me during my experimental work all this year. Thanks a lot Maria; I appreciate all the help.

I would also like to thank Michalis Loulakis for his guidance during my first training in the lab. Thanks to him, the maintenance of the laser system made our experimental work easier. In addition many thanks to Tasos Koulouklidis for the great collaboration we had during my experiments that presented in this thesis. Many thanks also to Paris Panagiotopoulos for his help and support during this year. Thank you all of you guys for your encouragement and the fun moments we had during this year of my master studies.

Many thanks also to my friends for the great moments we had outside the scientific environment.

Finally, I would like to thank my family for their support all these years of my studies.

Abstract

The THz frequency range is one of the most interesting regions of the electromagnetic spectrum. THz radiation lies between the far-infrared and the microwave region, in a frequency interval from 0.1 THz to 30 THz. Historically, it is known as the “THz gap” due to the lack of coherent sources in this frequency range. Nevertheless since the last two decades numerous works have been done on coherent sources and it is now possible to access the THz frequency region of the electromagnetic spectrum.

Many non-metallic and non-polar materials are transparent to THz radiation, due to the vibrational and rotational transitions of many molecules that lie in the THz frequency range. Furthermore, THz radiation is non-ionizing (\sim meV) and is absorbed highly by water. These unique properties of this radiation have been revealed, suggesting the development of promising applications either spectroscopic or imaging. In this work which is divided into two parts, we present the application of THz Time-Domain Spectroscopy (THz-TDS) in two different scientific fields.

In the first part of the thesis, applications of THz-TDS in food inspection are presented. Specifically studies have been performed in distinguishing different antibiotics and acaricides residues in honey. The antibiotics and acaricides have been optically characterized in the THz frequency range between 0.3 THz and 8 THz and most of them showing specific fingerprints in this frequency range. The main spectral features of two antibiotics were still detectable when they were mixed with pure honey. These residues in honey can be detectable in concentrations up to 0.1%. These results indicate that THz-TDS can be used in the production line in the near future.

In the second part of the thesis, a number of different excipients constituting a pharmaceutical tablet have been characterized in the THz frequency range. These preliminary studies aim to use THz-TDS as an efficient tool for detecting the dosages of the excipients in the production line. This work is still in progress and is conducted in cooperation with a pharmaceutical industry.

Table of contents

Acknowledgments	3
Abstract	4
Table of contents	5
1. Introduction	7
1.1 Overview of Terahertz (THz) science.....	7
1.1.1 Definition and characteristic features of THz radiation	7
1.1.2 Applications of THz radiation	10
1.2 THz sources.....	14
1.2.1 Photoconductive antennas	14
1.2.2 Optical rectification in nonlinear media.....	16
1.2.3 Two-color filamentation in air.....	18
1.3 THz Detection	18
1.3.1 Pyroelectric detector.....	19
1.3.2 Heterodyne detector.....	19
1.3.3 Photoconductive sampling.....	21
1.3.4 Electro-optic sampling.....	22
2. Terahertz Time-Domain Spectroscopy (THz-TDS)	23
2.1 THz experimental setup	23
2.2 THz emission through two-color filamentation in air	24
2.3 THz detection through electro-optic sampling	26
2.4 Data analysis.....	36
3. Terahertz spectroscopy of honey	41

3.1	THz spectroscopy in food industry	41
3.2	THz spectroscopy of honey: Qualitative and quantitative approach	42
3.2.1	Experiment and sample preparation	42
3.2.2	Results and discussion.....	44
4.	Terahertz spectroscopy of pharmaceutical products	51
4.1	THz spectroscopy and pharmaceutical applications	51
4.2	THz spectroscopy of pharmaceutical products: Qualitative and quantitative approach.....	52
4.2.1	Experiment and sample preparation	52
4.2.2	Results and discussion.....	53
	References	56

1. Introduction

1.1 Overview of Terahertz (THz) science

1.1.1 Definition and characteristic features of THz radiation

In the last years, one of the most interesting regions of the electromagnetic spectrum for exploring a number of scientific phenomena lies in the THz frequency range. THz radiation lies in a frequency interval from 0.1 THz to 30 THz and it was first isolated in 1897 by Heinrich Rubens [1]. These frequencies correspond to a wavelength range from 3 mm to 10 μm , photon energy from 0.4 meV to 120 meV and to an equivalent black body radiation with temperatures between 4 K and 1200 K. A more analytical approach about the conversion between these parameters is given at Table 1. The first wording of the term "THz" is attributed to Fleming in 1974 and the term was used to describe the spectral line frequency coverage of a Michelson interferometer [2]. However, this electromagnetic region, shown in Figure 1, remained unexplored for a long time.

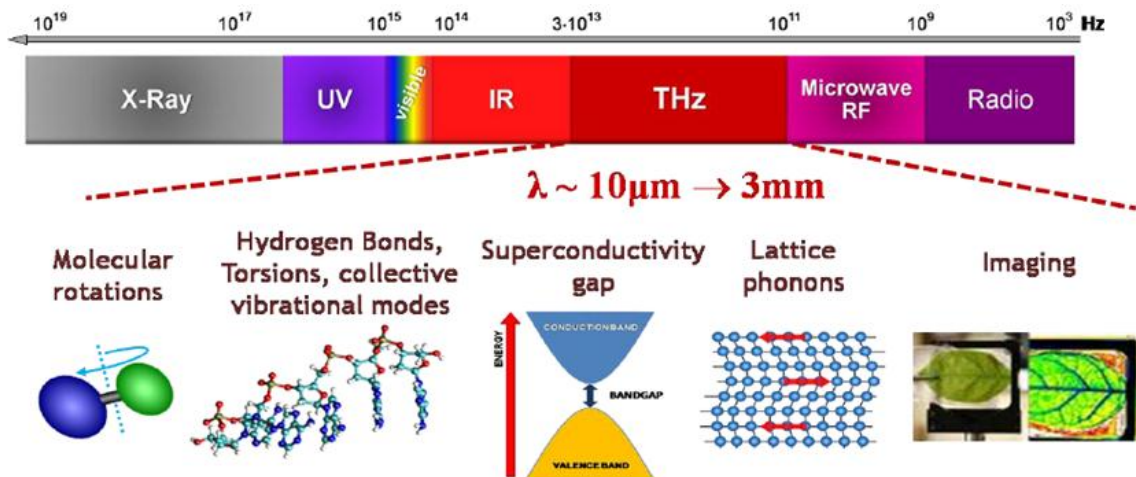


Figure 1: The electromagnetic spectrum in frequency domain. The THz region is depicted in dark red and its applications and corresponding spectroscopic modes are presented.

Despite the interest in this electromagnetic area, THz radiation has remained one of the most untapped and least understood regions of the electromagnetic spec-

trum, compared to the relatively well developed science and technology in the microwave and optical frequencies. The term “THz gap” resulted from the limits of the electron velocities which prevent electronic devices to operate above a few hundred GHz, and from thermal energies that limit the smallest electronic transitions useful for lasing, preventing solid-state lasers to operate below a few hundred THz.

Radiation Frequency (THz)	Wavelength (μm)	Wavenumber (cm^{-1})	Energy (meV)	Temperature (K)
0.5	600	16.66	2.066	24
1	300	33.33	4.133	48
3	100	100	12.4	144
6	50	200	24.8	288
8	37.5	266.66	33.066	384
10	30	333.33	41.333	480

Table 1: Conversion of parameters that characterize the electromagnetic waves in the THz regime.

The first demonstration of a coherent emission and detection of broadband THz pulses in the late 1980’s allowed to routinely access this part of the electromagnetic spectrum [3]. Thus, the unique properties of THz radiation have been revealed, suggesting the development of promising applications.

First of all, THz waves have longer wavelengths than visible and infrared waves. This means that THz waves are less affected by Mie scattering. As a consequence, various nonpolar dielectric materials such as paper, plastic, wood, clothing, leather, and ceramics which are usually opaque to both visible and infrared radiation are transparent to THz radiation. Instead, it is totally reflected from metallic surfaces and partially reflected from interfaces between non-metallic materials with different refractive indices, enabling objects to be detected beneath various surfaces.

Secondly, THz waves have low photon energy (~ 4 meV at 1 THz) and thus THz radiation can be used for studying a number of materials, such as biological, in a non-ionizing and non-destructive way. A typical X-ray photon has energy in keV range, which is one million times higher than a THz photon, making THz radiation an excellent diagnostic tool.

As shown in Figure 2, a number of molecular rotations, low frequency bond vibrations and crystalline phonon vibrations are present in this frequency range. Thus, many molecules exhibit strong absorption features in the THz frequency range. These unique rotational and vibrational responses of materials provide information that is generally absent in optical, X-ray and nuclear magnetic resonance images. Consequently, molecules exhibit fingerprints which allow their spectroscopic identification [4].

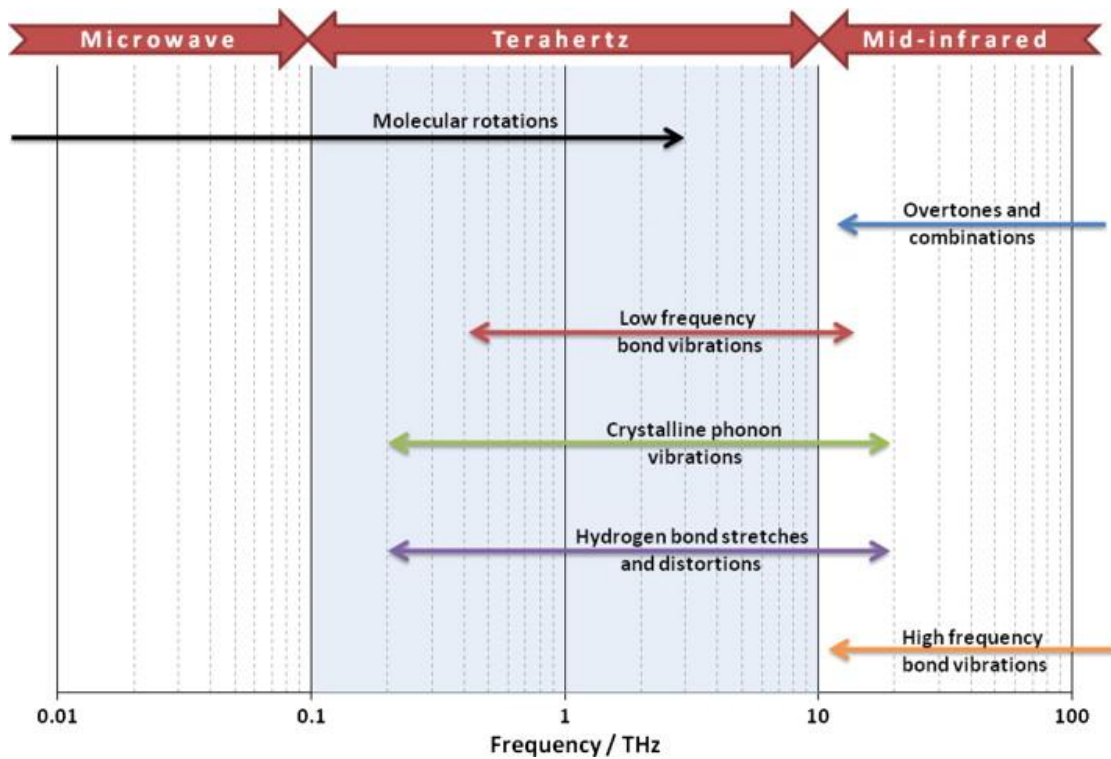


Figure 2 : Various molecular interactions in the THz frequency region [5].

THz pulses can be detected coherently, by the sampling measurement of their electric field, giving a direct access to the amplitude and the phase of the radiation. This gives access to absorption and dispersion spectroscopy of many materials, giving us also chemical and structural information [6].

Finally numerous solid state phenomena lie within the THz range. For example, the band gaps of superconductors, the phonon modes of most semiconductors and crystals have frequencies in the THz regime [7]. Consequently, THz radiation is a promising tool for fundamental studies and deeper understanding of solid state phenomena.

1.1.2 Applications of THz radiation

The applications of THz technology, both fundamental and applied, can be separated into two main categories: THz imaging and spectroscopy. Both techniques are applied in a variety of scientific fields such as medical science, biology, pharmaceutical industry, food industry, material science, art conservation, security and astronomy (Figure 3).

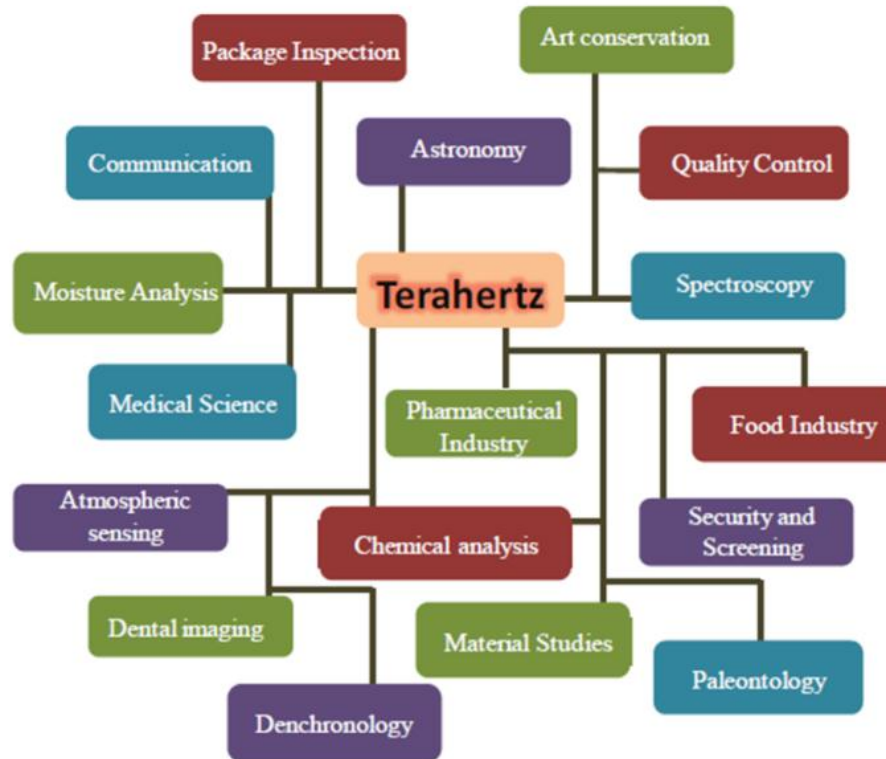


Figure 3: THz spectroscopy and imaging applications.

Medical science is a fertile field for THz imaging because unlike X-rays, THz radiation is not harmful to the biological tissues. The progress of THz imaging over the last years makes it now a significant body of research in its application to biomedical problems with the possibility of developing it into medical imaging modality in the future. Until now, there are a lot of studies in which THz pulsed imaging was used to distinguish cancerous from healthy tissues. The contrast between them is attributed to their different hydration levels [8-10]. An example of THz imaging of skin cancer is represented in Figure 4, where is shown the correspondence between a clinical photo, a THz image and a histological image. However, it is not yet known if THz imaging would be able to discriminate different types of cancer or even to discriminate cancerous from non-cancerous lesions. THz imaging as a diagnostic tool is still in initial stage and the

systems based on it, still require significant improvements and development before they can be accepted as non-invasive diagnostic tools by the medical community.

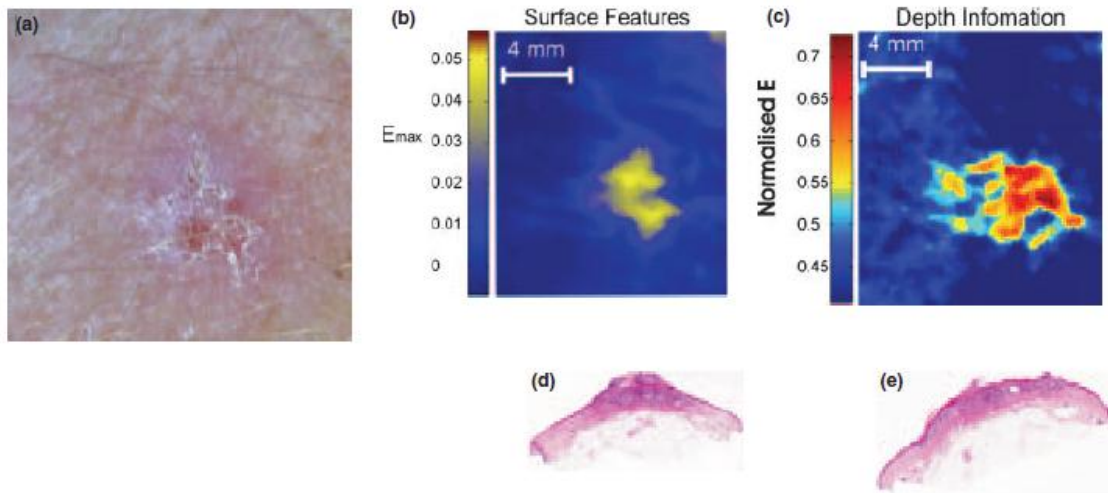


Figure 4: In vivo measurement of basal cell carcinoma with an invasive component. (a) Clinical photograph of the lesion. (b) and (c) Terahertz images. (d) and (e) Representative histology section showing acute inflammatory crust corresponding to terahertz image (b) and (c) respectively [8].

Furthermore, terahertz waves are highly sensitive to polar molecules, like water. Recently, it has been demonstrated that THz imaging can be used as an excellent non-invasive tool for mapping the hydration levels in tissues. In vivo THz imaging measurements on the stratum cornea in the eye, have shown that compared to other existing clinical techniques which are either invasive or use an indirect approach for quantifying water content, THz imaging is a promising tool for such applications [11].

Another research field of the THz technology is Security screening, mainly focused on safety in public spaces. Its use at airports underlines the need for quick, reliable and safe personal screening. The radiation in this frequency regime has a unique combination of properties; THz radiation is non-ionizing and also many materials are transparent to it, as it was mentioned in the previous section. THz technology can be used as a safe alternative solution for non-invasive imaging of humans, offering the possibility to screen and locate concealed objects or materials as illustrated in Figure 5 and Figure 6 [12]. THz imaging has also been successfully employed to screen explosives and drugs which have also distinct fingerprints in the THz spectrum [13].

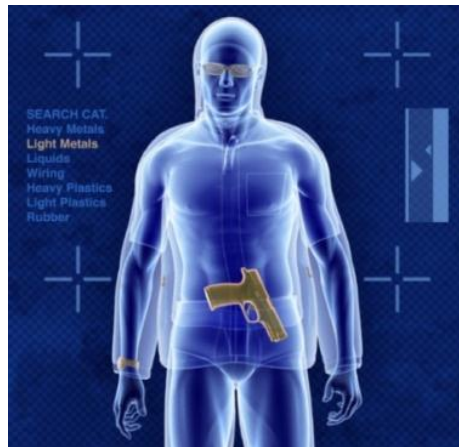


Figure 5: Security screening with THz radiation.

(<http://physicsworld.com/cws/article/news/2012/jun/12/new-tuner-could-bring-terahertz-to-the-masses>)

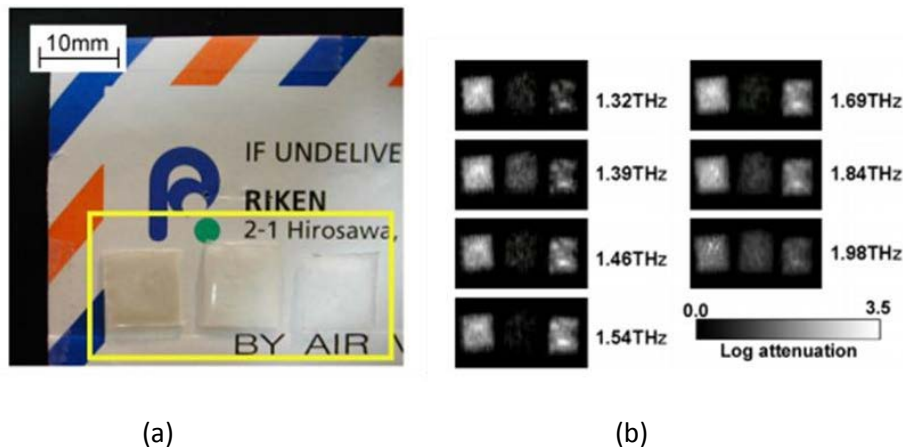


Figure 6: (a) Bags contain from left to right: MDMA, aspirin, and methamphetamine. (b) Seven multispectral THz images generating a matrix [13].

THz radiation can provide also additional details and complementary spectroscopic data related to art conservation. It can be used to provide information about the materials existing below the layers of the paint, such as preparation layers. In addition, it provides depth information from the paint layers. An ultimate goal of the THz technology in this field is the investigation of mural wall paintings where X-rays cannot be easily applied [14-16]. Except of using THz waves for non-invasive imaging, THz spectroscopy plays a significant role for the analysis of various materials of cultural heritage interest. The spectra of various historical and modern pigments and binders have been already studied. A lot of them exhibit characteristic fingerprints in the THz frequency range [16-18]. With this technique most of these materials used in paintings can be identified alone, as paint, or in a combination with pigments and binders. Two charac-

teristic examples of spectroscopy and THz imaging are illustrated in Figure 7 and Figure 8.

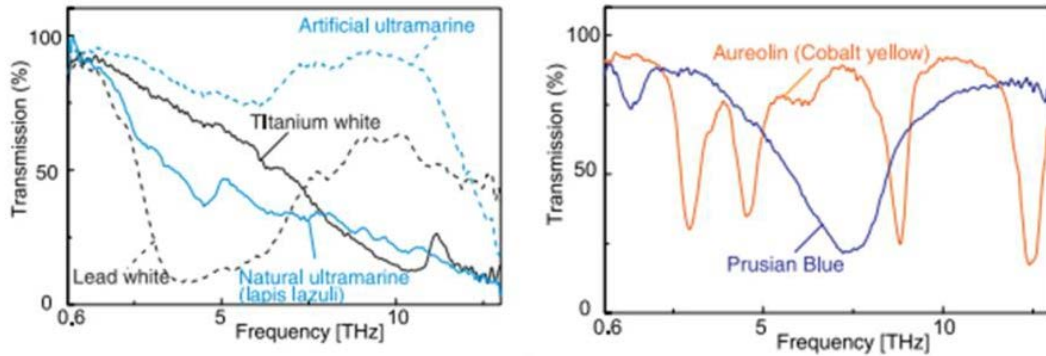


Figure 7: Examples of THz spectra of different pigments [17]

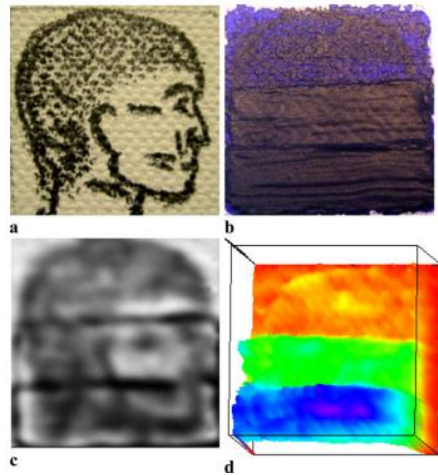


Figure 8: Photograph of (a) the graphite sketch and (b) the ultramarine painted surface with three different thicknesses, (c) transmission THz image at 1 THz, (d) 3D THz map of the sample obtained using the THz main pulse time delay, the blue color indicates an increase of the optical pathway [14].

In pharmaceutical industry, THz imaging has progressed as a new technique which includes information about coating thickness and uniformities in coated pharmaceutical tablets. Supplementary, THz spectroscopy as a new technology has gained increasing attention in the study of pharmaceutical materials and process understanding during the last decade. The need for spectroscopic analysis of pharmaceutical tablets and also the dosage of the excipients makes THz spectroscopy an excellent candidate for non-destructive imaging and analytical spectroscopy during the production process and control in terms of safety [19-21].

The presence of antibiotic residues in food is becoming a growing concern among consumers. As a result, there is need for development of new, rapid, techniques for antibiotic residues detection, and THz spectroscopy is a novel and very promising technique for this purpose. The ability of THz waves to pass through a wide variety of packaging materials, combined with their ability to characterize the molecular structure of many substances makes THz spectroscopy an attractive analytical tool for enhanced monitoring in food production line. Especially in food inspection there are several reports until now related to detection of antibiotic residues in food matrices, detection of pesticides in food powders (potato, rice, root) or just spectroscopic characterization of eatable products such as vegetable oil [22].

All the aforementioned applications show the wide range of THz waves. In the next sections, different approaches for the generation and detection of THz radiation are described.

1.2 THz sources

Two of the most common broadband pulsed techniques for the emission of THz radiation using ultrafast laser pulses are the use of photoconductive antennas and optical rectification in nonlinear media. The photoconductive approach uses high-speed photoconductors as transient current sources and the optical rectification approach uses electro-optic crystals as rectification media. More details about these approaches are given in the two first sections. Furthermore, a brief introduction will be given for the technique of THz emission through filaments formed by high intensity ultrashort laser pulses. This technique has received considerable attention in the last few years as novel table-top intense THz source and is applied for the generation of intense THz pulses used for accomplishing the experiments of this work.

1.2.1 Photoconductive antennas

The use of photoconductive antennas is probably the most widely used method for the generation of THz pulses. A photoconductive antenna consists of two metal electrodes that are deposited on a semi-insulating semiconductor substrate with a gap between these two electrodes as it is illustrated in Figure 9. All the photoconductive antennas used as THz emitters are based on the same principle. For the generation of

THz pulses, an external bias voltage is applied across the electrodes. Since the substrate is semi-insulating, electric energy is stored in the gap area.

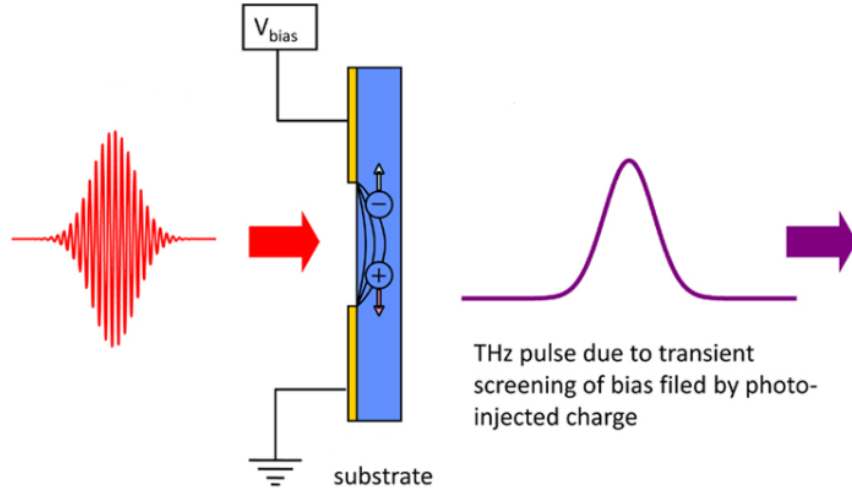


Figure 9: THz emission from photoconductive antenna.

An incoming ultrafast laser pulse with photon energy above the band gap of the semiconductor wafer excites free carriers to the conduction band. These free carriers are immediately being accelerated due to the presence of the bias field inside the emitter and produce a photocurrent. This fast time varying current radiates THz electromagnetic waves. Finally, the photoexcited free carriers are trapped or recombine and the current density returns to its steady value. Then the THz emitter is prepared for the emission of the next pulse. Since electrons usually have much higher mobility than holes, the contribution of holes can be ignored in most cases. The current density is described as [23]:

$$J(t) = N(t)e\mu E_b \quad (1.1)$$

where N is the density of photocarriers, e is the elementary charge, μ is the mobility of electron, and E_b is the bias electric field. The photocarrier density N is a function of time, whose format is determined by the laser pulse shape and the carrier lifetime. Since the photocurrent varies in time, it generates electromagnetic pulse, whose electric field is approximately:

$$E_{THz} = \frac{1}{4\pi\epsilon_0} \frac{A}{c^2 z} \frac{\partial J(t)}{\partial t} = \frac{Ae}{4\pi\epsilon_0 c^2 z} \frac{\partial N(t)}{\partial t} \mu E_b \quad (1.2)$$

where A is the area in the gap illuminated by the laser light, ϵ_0 is the vacuum permittivity, c is the speed in vacuum, and z is the distance between the field point and the THz source. To derive the second equation, the field point is assumed located at normal to the photoconductive antenna and the distance between the field point and the source is much larger than the dimension of the photoconductive antenna.

The energy of the THz pulse comes from the electric energy stored across the gap rather than the optical pulse energy. Since the radiating energy comes from the stored energy in the form of the static bias field, the THz radiation energy increases with the bias and optical fluency [24].

1.2.2 Optical rectification in nonlinear media

Optical rectification, which is also a widely used method for the emission of THz radiation, is a second-order nonlinear optical process used for the generation and also the detection of THz radiation. It is a process, similar to the linear electro-optic effect, which occurs only in crystals that are non-centrosymmetric and sufficiently transparent at THz and optical frequencies. As illustrated in Figure 10, one femtosecond laser pulse is enough to stimulate optical rectification radiation. In order to describe this phenomenon, it is convenient to treat it as a special case of a difference frequency generation, where optical photons with close frequencies ω_1 and ω_2 produce a far-infrared photon with frequency $\omega = \omega_1 - \omega_2$. The wide spectral bandwidth of the incident femtosecond laser pulse causes a fast change in the electrical polarization inside the crystal, which in turn emits THz radiation. Mathematically, the polarization P can be expanded into a power series of the electric field E [23]:

$$P(r,t) = \chi^1 E(r,t) + \chi^2 : E(r,t)E(r,t) + \chi^3 : E(r,t)E(r,t)E(r,t) + \dots \quad (1.3)$$

where $\chi^{(n)}(r,t)$ is the n th-order nonlinear susceptibility tensor. Optical rectification comes from the second term of the above equation. If the incident light is plane wave, then E can be expressed as:

$$E(t) = \int_0^{+\infty} E(\omega) \exp(-i\omega t) d\omega + c.c. \quad (1.4)$$

By substituting the first equation into the second, the polarization for optical rectification is given by:

$$\begin{aligned}
P_{OR}^{(2)} &= 2\chi^{(2)} : \int_0^\infty \int_0^\infty E(\omega_1)E^*(\omega_2)\exp[-i(\omega_1 - \omega_2)t]d\omega_1d\omega_2 \\
&= 2\chi^{(2)} : \int_0^\infty \int_0^\infty E(\omega + \Omega)E^*(\omega)\exp[-i\Omega t]d\Omega d\omega
\end{aligned} \tag{1.5}$$

where Ω is the frequency difference of two optical frequency components. In the far field, the radiated electric field $E_r(t)$ is proportional to the second derivative of $P_{OR}^{(2)}$ with respect to time t :

$$E_r(t) \propto \frac{\partial^2}{\partial t^2} P_{OR}^{(2)}(t) \tag{1.6}$$

Many factors, such as materials, crystal orientation, thickness, absorption and dispersion, diffraction, phase matching, and saturation, affect the radiation efficiency, waveform, and frequency distribution. Phase matching is the most important factor for nonlinear processes such as optical rectification and requires conservation of energy and momentum. It is satisfied in THz wave generation when the crystal's group refractive index for the femtosecond laser pulse is equal to the phase refractive index for the THz pulse. Only when phase matching is satisfied, all three waves participating in the optical rectification process can be kept in phase leading to maximum energy conversion along the light propagation; otherwise phase mismatch leads to a phase walk off while propagating.

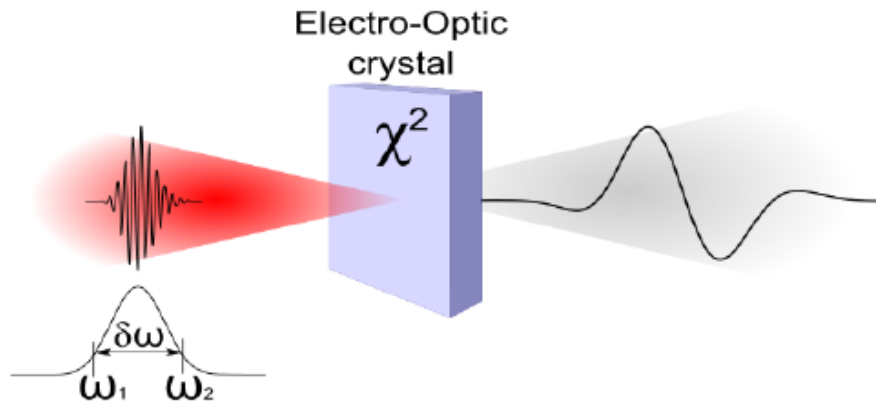


Figure 10: THz emission through optical rectification process.

1.2.3 Two-color filamentation in air

THz wave generation in ambient air has attracted considerable attention the last years. Figure 11 shows a schematic representation for the THz wave generation through mixing the fundamental and the second harmonic beam pulses of a high power, ultra-fast laser. The second harmonic beam is generated by focusing an intense laser beam through a BBO crystal which is the widely used nonlinear crystal for second harmonic wave generation. Both the second harmonic beam and residual fundamental beam propagate in the same direction and the THz emission is the result of a transversal plasma photocurrent produced from a synthesized 2-color asymmetric laser field. A more analytical approach will be given in the following chapter.

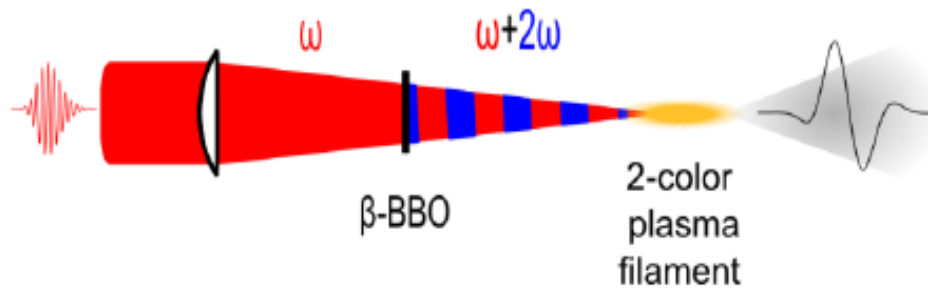


Figure 11: THz emission through two-color filamentation process in air [25].

1.3 THz Detection

Just as there are many different methods for generating THz radiation, there are also a number of different ways in which THz waves can be detected. THz detection systems can be divided into two categories:

- *Incoherent detection systems*, which allow only the signal's amplitude detection and are broadband detection systems such as pyroelectric detector, bolometer, Golay cells. Their main advantage is the relative operation simplicity without the need of adjustment in wide frequency band.
- *Coherent detection systems*, which allow detecting not only the amplitude of the signal but also its phase such as heterodyne receiver, photoconductive antennas, electro-optic sampling. This feature is important from the point of view of increasing the information received from the object under study. It also allows us to realize higher detector sensitivity and spectral resolution characteristics.

1.3.1 Pyroelectric detector

Pyroelectricity is the ability of certain anisotropic materials to generate an electrical voltage when they are heated or cooled. Their change in temperature modifies the positions of the atoms within the crystal structure, such that the polarization of the material changes. This change in polarization may be observed as an electrical signal if electrodes are placed on opposite faces of a thin slice of the material to form a capacitor as is shown in Figure 12. The sensor will only produce an electrical output signal when there will be a change in the temperature. If the temperature stays constant, the pyroelectric voltage gradually disappears due to leakage current. Pyroelectric effect is sensitive only to heat, not to wavelength and wavelength selection is made through selection of appropriate window material. Finally, pyroelectricity can be visualized as one side of a triangle, where each corner represents energy states in the crystal: kinetic, electrical and thermal energy. The side connecting the thermal and electric energies represents the pyroelectric effect. The side connecting the electrical and mechanical energies represents the piezoelectric effect and the side linking mechanical and thermal energies represents the thermo-electric effect.

For terahertz applications that do not require high sensitivity, pyroelectric detectors have been offered [26]. Ferroelectric materials such as Lithium Tantalate, exhibit a large spontaneous electrical polarization varying with temperature.

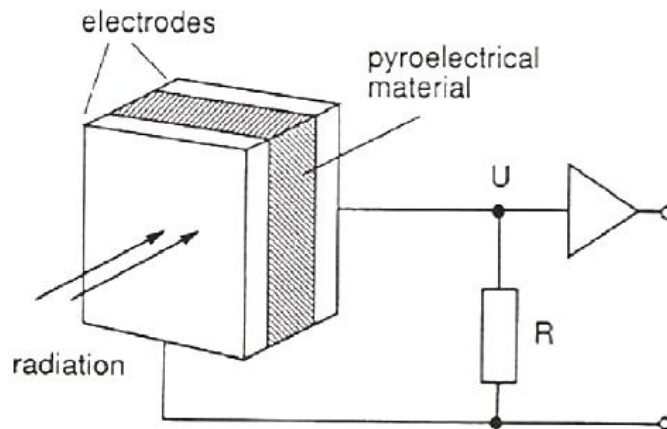


Figure 12: Schematic representation of a pyroelectric detector.

1.3.2 Heterodyne detector

Heterodyne detection is a coherent detection method by non-linear mixing with radiation of a reference frequency. In this method, a weak input signal which is most

commonly either radio waves or light is mixed with some strong local oscillator wave which is the reference signal. Then the input signal and the local oscillator are superimposed at a frequency mixer. The mixer, which is commonly a (photo-) diode, has a non-linear response to the amplitude, that is, at least part of the output is proportional to the square of the input. Finally, the resulting mixing product is then detected, often after filtering out the original signal and the local oscillator frequency. A schematic representation of a heterodyne detection system is illustrated in Figure 13.

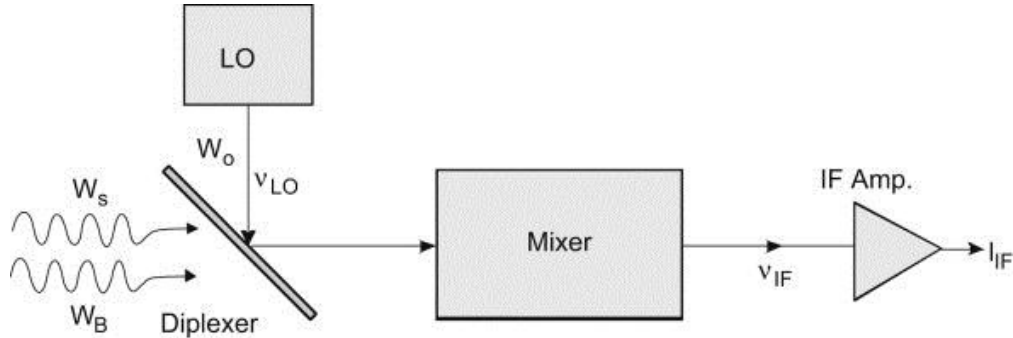


Figure 13: Schematic representation of heterodyne detection.

The received signal can be represented as:

$$E_{sig} \cos(\omega_{sig}t + \varphi) \quad (1.7)$$

and the signal from the local oscillator can be represented as:

$$E_{LO} \cos(\omega_{LO}t) \quad (1.8)$$

Approximately, the output I of the detector is proportional to the square of the amplitude:

$$I \propto \left(E_{sig} \cos(\omega_{sig}t + \varphi) + E_{LO} \cos(\omega_{LO}t) \right)^2. \quad (1.9)$$

The output I of the detector has high frequency ($2\omega_{sig}$ and $2\omega_{LO}$) and constant components. In heterodyne detection, the high frequency components and usually the constant components are filtered out, leaving the intermediate frequency at $\omega_{sig} - \omega_{LO}$. The amplitude of this last component is proportional to the amplitude of the signal radiation. With appropriate signal analysis the phase of the signal can be recovered as well.

1.3.3 Photoconductive sampling

Photoconductive antennas are widely used not only for generating THz radiation but also for their coherent detection. For this purpose, a photoconductive antenna with an identical structure to an antenna emitter can be used as shown in Figure 14. The only major difference is that as a detector, the two electrodes of the antenna are connected to a current sensor in order to measure the transient current generated by an optical pulse and biased by the THz field. In the THz detection system by controlling the time delay between the THz pulse and the optical probe pulse, the electric field across the strip line of the photoconductive antenna at any given time is sampled by the optical probe pulse which serves to generate transient photocarriers in the substrate at that specific time. This measurable average current is in the order of several hundred picoamperes down to tens of nanoamperes. The induced THz field current is [23]:

$$\bar{J} = \bar{N}e\mu E(\tau) \quad (1.10)$$

Here \bar{N} denotes the average electron density, and τ is the temporal delay between probe and the THz pulse. By scanning the temporal delay, the THz pulse waveform, as a function of τ , is recorded. Typically the period of the THz oscillation is about one picosecond (ps). The measurement provides information not only about the amplitude, but also for the phase of the THz pulse.

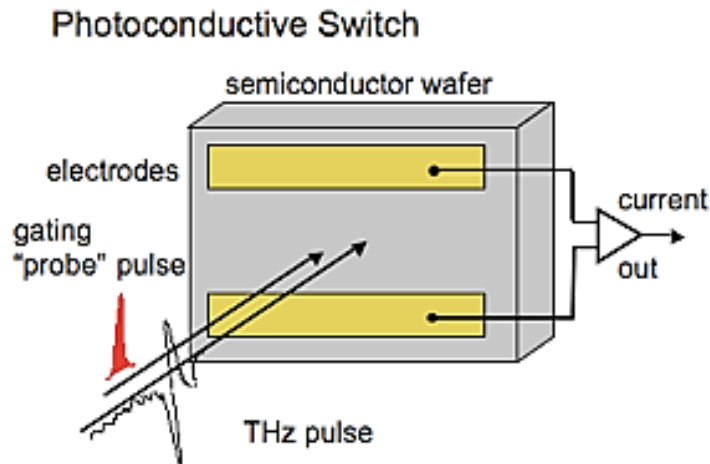


Figure 14: THz detection with photoconductive antenna.

1.3.4 Electro-optic sampling

Another common method for the detection of THz radiation is the electro-optic sampling [27] which is based on the linear electro-optic effect (Pockels effect). In essence, the incident THz pulse induces a birefringence in an electro-optic medium which is proportional to the electric field of the pulse. This varying birefringence can be measured by observing the change in polarization state of an optical probe pulse which is travelling through the electro-optic medium. By measuring the degree of the induced birefringence as a function of delay between the terahertz pulse and the optical probe pulse, the terahertz electric field is mapped. A schematic representation is shown in Figure 15. More details about this detection approach will be given in chapter 2.

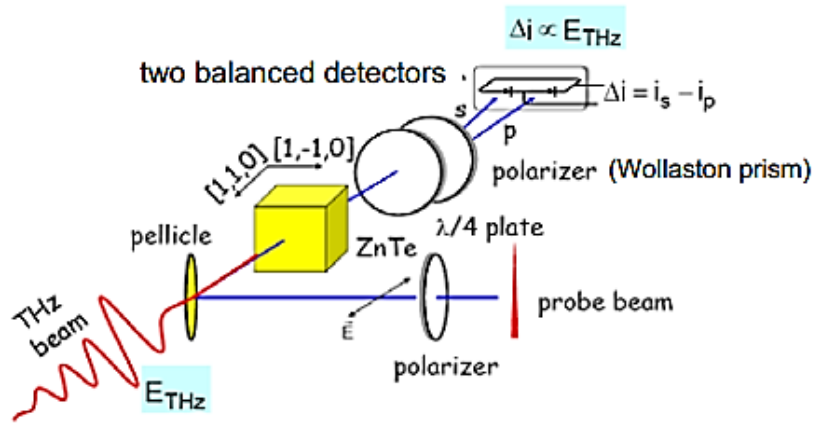


Figure 15: Schematic representation of electro-optic sampling.

2. Terahertz Time-Domain Spectroscopy (THz-TDS)

2.1 THz experimental setup

In the previous chapter, we have been introduced the classic approaches for the emission and detection of THz radiation. In this chapter, the basic requirements in order to build a THz time domain spectrometer (THz-TDS) are presented. Our homemade THz-TDS system is based on a pump-probe, coherent detection approach. A powerful amplified kHz Ti:Sa laser system delivering 35 fs pulses at 800 nm central wavelength and energy of 2.3 mJ per pulse is used. Using a dielectric beam splitter, the initial beam is split in two arms (10% and 90%, respectively); a pump beam containing most of the energy and a weaker probe beam which will be used to measure the emitted THz radiation. The first arm is focused in ambient air after partial frequency doubling in a Barium-borate (BBO) crystal to produce a two-color filament and subsequently, THz radiation. Then, a set of four parabolic mirrors is used to collect, collimate, focus and bring the THz beam to the detection crystal as depicted in Figure 16.

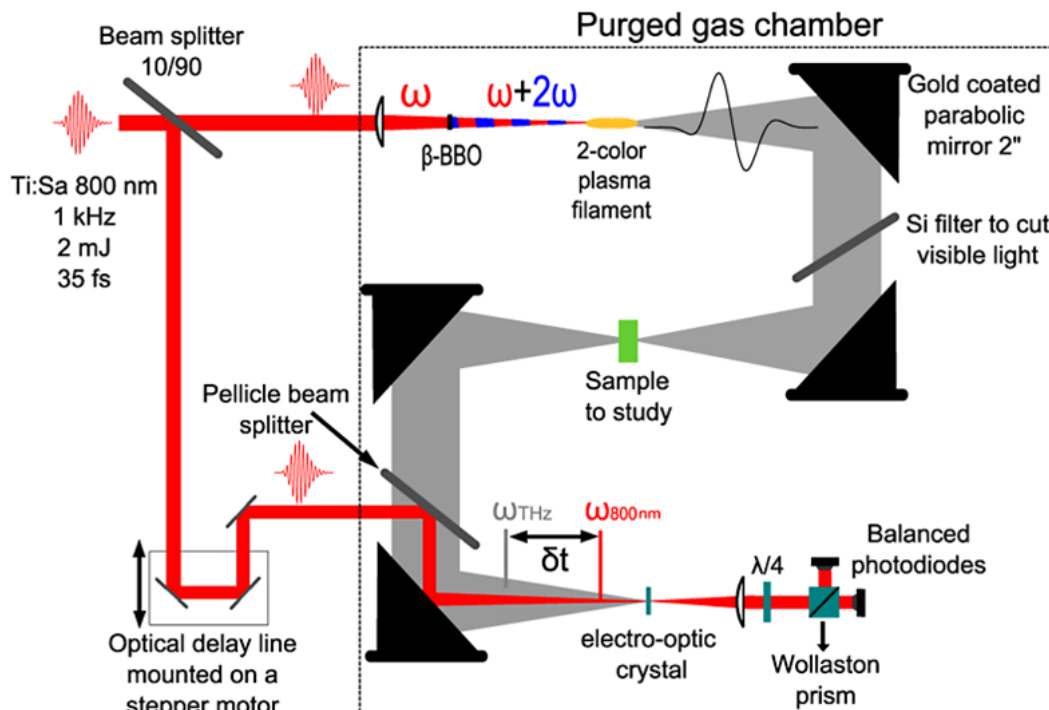


Figure 16: Schematic representation of the THz experimental setup.

A high resistivity silicon wafer (0.5 mm thick) is used to stop the remaining optical light. For the detection of THz radiation, the second arm of the initial beam is used to probe the THz field using electro-optic sampling. The probe beam passes through an optical delay line which is mounted on a step motor of femtosecond resolution. A pellicle beam splitter (R: T=25:75, ~5 μm thick,) is used to introduce the optical beam in a collinear way with the THz beam. A balanced detection is used to measure the induced phase delay on the probe beam. Finally, the whole setup is enclosed in a purged gas (e.g. N₂) chamber for eliminating THz absorption from water vapor.

2.2 THz emission through two-color filamentation in air

In the last 20 years, filaments formed by high intensity ultrashort laser pulses have received considerable attention as novel sources for radiation [28]. At high incident power (GW to TW) and intensities, the air cannot be considered linear anymore. The filamentation process then can be described by the action of two main nonlinear physical effects. On one hand, the optical Kerr effect acts against diffraction and tends to focus the beam on itself. The origin of self-focusing is related with the nature of the refractive index. In the presence of a strong laser field, the refractive index of air is not only dependent on the frequency of the laser field, but also on its spatio-temporal intensity distribution: $n(I) = n_o + n_2 I$ where n_2 is its nonlinear refractive index. On the other hand during self-focusing, the beam's intensity becomes higher and reaches levels that are sufficient to ionize the surrounding gas. This ionization effect reduces the local refraction index of the medium and leads to beam defocusing. This effect acts as a negative defocusing lens, preventing the beam from collapsing. The dynamical equilibrium between these two phenomena results in the formation of a filament as schematically represented in Figure 17.

The emitted radiations from this process include high harmonics of the fundamental laser pulse, soft and hard X-rays, as well as THz radiation at the low frequency side of the E/M spectrum. Especially, two-color filamentation in air induced by a femtosecond laser pulse (fundamental wave) and its second harmonic wave has been demonstrated as an efficient technique for generating intense THz waves [29].

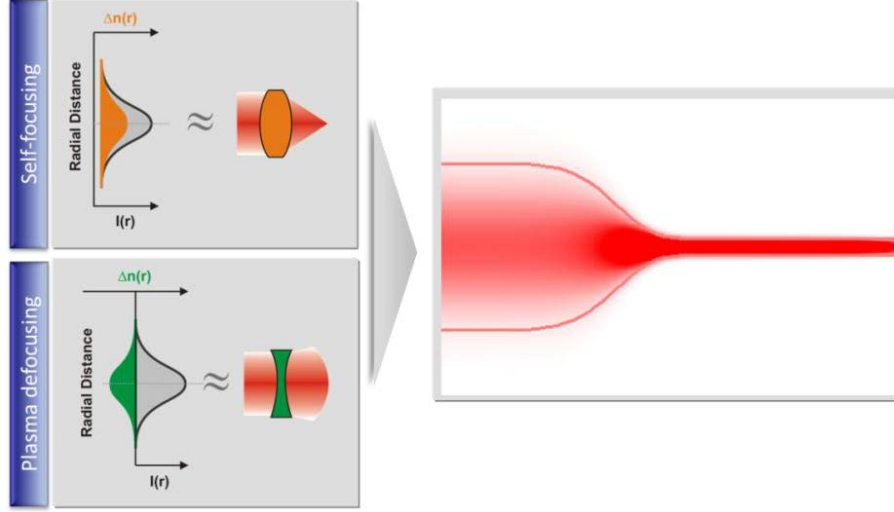


Figure 17: Schematic representation of the filamentation process.

There are typically two models used to explain the nonlinear optical processes responsible for the THz emission in air.

The first model is the four-wave mixing (FWM) model and the other is the asymmetric transient current model. In the first case, the FWM process is related to $\chi^{(3)}(\omega_{THz} : 2\omega + \omega_{THz}, -\omega, -\omega)$ and the emitted THz electric field can be expressed as [30]:

$$E_{THz}(t) \propto \chi^{(3)} E_{2\omega}(t) E_{\omega}^*(t) E_{\omega}^*(t) \cos(\varphi) \quad (2.1)$$

At relatively low input laser power, the THz emission was shown to increase linearly with the intensity of the fundamental pulse (ω) and followed the square root of the intensity secondary harmonic (2ω), as predicted from the following equation:

$$E_{THz} \propto \chi^{(3)} \sqrt{I_{2\omega}} I_{\omega} \cos(\varphi) \quad (2.2)$$

On the other hand, according to the photocurrent model intense THz pulses are emitted through a 2-color filament as the result of a net transverse current is formed in the plasma channel. For appropriate phase between the ω and 2ω , an asymmetric synthesized laser electric field is formed and strips off the free electrons towards the same direction [31]. For this model the synthesized laser field is:

$$E_L(t) = E_{\omega} \cos \omega t + E_{2\omega} \cos(2\omega t + \theta) \quad (2.3)$$

When the electrons are ionized, the external laser electric field accelerates them at a velocity of:

$$v(t) = -\frac{e}{m_e} \int_{t_0}^t E_L(t) dt \quad (2.4)$$

Assuming that the initial electron velocity is zero, the drift velocity of is given by the following equation:

$$v_d(t') = \frac{eE_\omega \sin(\omega t')}{m_e \omega} + \frac{eE_{2\omega} \sin(2\omega t' + \theta)}{2m_e \omega} \quad (2.5)$$

As a result, for $\theta = \pi/2$ the symmetry is broken and a net current is formed which is given by the equation:

$$J_\perp(t) = \int_{t_0}^t e v_e(t, t') N_e(t) dt' \quad (2.6)$$

where N_e is the electron density calculated from the ionization rate equation. The THz electric field is derived from the electron current density:

$$E_{THz} \propto \frac{dJ_\perp(t)}{dt} = e \frac{dN_e(t)}{dt} v_d(t) \quad (2.7)$$

2.3 THz detection through electro-optic sampling

Electro-optic sampling is a coherent optoelectronic technique of optical sampling in which the propagation of THz waves through optically active crystals leads to the linear electro-optic effect or Pockels effect, which is the basis of electro-optic detection techniques. In electro-optic sampling, the THz electric field is measured by modulating an optical probe pulse inside an electro-optic (e.o.) crystal, where it changes the polarization ellipsoid of its refractive index. The linearly polarized probe pulse co-propagates inside the crystal with the THz pulse (pump), and its phase is modulated by the refractive index change. The existence of the THz field changes the birefringence of the electro-optic crystal, causing the refractive index difference for polarizations along

different axes of the crystal. This polarization change is converted to intensity change by an analyzer, for example a Wollaston prism. Usually a pair of balanced photodiodes is used to suppress the common laser noise while the signal is doubled. A more detailed description about the Pockels effect and generally the electro-optic detection will be given below [32].

Crystals are classified as being either isotropic or anisotropic depending upon their optical behavior and whether or not their crystallographic axes are equivalent. A schematic representation of both isotropic and anisotropic media is illustrated in Figure 18.

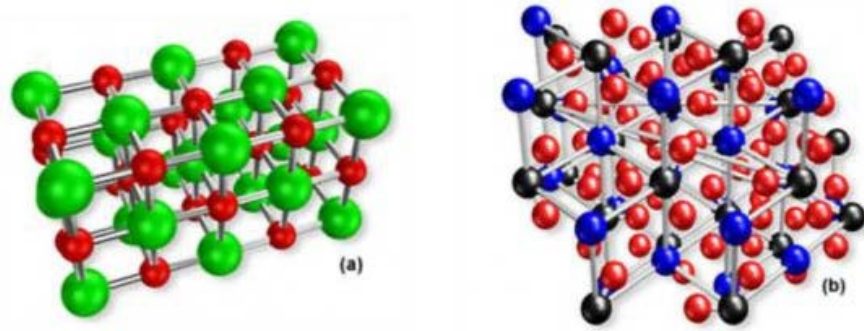


Figure 18: Schematic representation of an (a) isotropic crystal (sodium chloride) and of an (b) anisotropic crystal (calcite).

In case of an isotropic medium, the polarization P induced by an electric field E is always parallel to the electric field vector and related to the field by a scalar factor, the susceptibility χ and the permittivity of free space ϵ_0 . Consequently, we can write the following equations about the electric polarization P and also for the electric displacement field D , for an isotropic medium:

$$P = \epsilon_0 \chi E \quad (2.8)$$

and
$$D = \epsilon_0 E + P = \epsilon_0 E + \epsilon_0 \chi E = \epsilon_0 (1 + \chi) E = \epsilon E \quad (2.9)$$

where
$$\epsilon = \epsilon_0 (1 + \chi) \quad (2.10)$$

is the dielectric permittivity of the medium. The value $1 + \chi$ is called the relative permittivity of the medium, and is related to the refractive index n , for non-magnetic media, by the following equation:

$$n = \sqrt{(1 + \chi)} \quad (2.11)$$

If the medium is anisotropic, the polarization P is not necessarily aligned with the electric field of the light, E . In a physical picture, this can be thought of as the dipoles induced in the medium by the electric field having certain preferred directions, related to the physical structure of the crystal, so the susceptibility is now a tensor. As a result, the previous equations for P and D must be written in this case as:

$$P_i = \varepsilon_o \chi_{ij} E_j \quad (2.12)$$

and

$$D_i = \sum_j \varepsilon_{ij} E_j \quad (2.13)$$

Here, the susceptibility χ_{ij} which is a tensor and depends on the choice of the coordinate system relative to the crystal lattice. Also, ε_{ij} is known as dielectric tensor. For simplicity, it is preferable to find a system, where χ_{ij} becomes a diagonal matrix, zeroing all components of the tensor except χ_{xx} , χ_{yy} and χ_{zz} . These axes (x , y , z axes) are in this case known as the principal axes of the crystal and will be orthogonal if all entries in the χ_{ii} tensor are real, corresponding to a case in which the refractive index is real in all directions. If they χ_{ii} are not all equal, the material will exhibit birefringence.

When light enters the optical axis of anisotropic crystals, it behaves in a manner similar to the interaction with isotropic crystals, and passes through at a single velocity. However, when light enters a non-equivalent axis, it is refracted into two rays (ordinary and extraordinary ray), each polarized with the directions oriented at right angles perpendicular to one another and traveling at different velocities. This phenomenon, which is represented in Figure 19, is termed double refraction or birefringence and is exhibited to a greater or lesser degree in all anisotropic crystals.

The phase velocity v_p of a plane electromagnetic wave in an anisotropic crystal, which is written as:

$$v_p = \frac{c}{\sqrt{\varepsilon}} = \frac{c}{n} \quad (2.14)$$

depends on the direction of propagation and the direction of polarization. Along a given direction of propagation, two orthogonal optical axes U_o and U_e with different phase

velocities and thus different refractive indices exist. The refractive indices of these two modes are commonly called n_o (for the ordinary ray) and n_e (for the extraordinary ray).

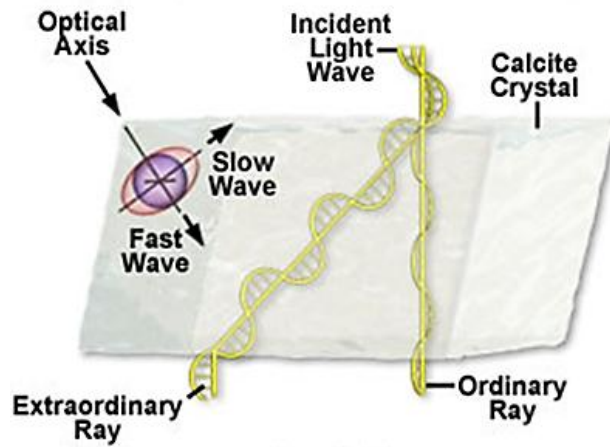


Figure 19: Schematic representation of double refraction into calcite crystal.

In order to find the indices of refraction n_o and n_e , it is convenient to define the index ellipsoid. If we assume that the medium is homogeneous, non-absorbing and magnetically isotropic, then the energy density can be written in terms of the dielectric tensor:

$$U = \frac{1}{2} E \cdot D = \frac{1}{2} \sum_{i,j} E_i \epsilon_{ij} E_j \quad (2.15)$$

In case we choose to work in a coordinate basis in which the dielectric tensor is diagonal, then the equation (2.15) takes on the simple form:

$$\frac{D_x^2}{\epsilon_x} + \frac{D_y^2}{\epsilon_y} + \frac{D_z^2}{\epsilon_z} = 2U \quad (2.16)$$

where ϵ_x , ϵ_y and ϵ_z are the principle dielectric constants ($\epsilon_x = \epsilon_{xx}$, etc.). If we define a dimensionless vector:

$$r = \begin{pmatrix} x \\ y \\ z \end{pmatrix} = \frac{D}{\sqrt{2U}} \quad (2.17)$$

and define the principal indices of refraction n_x, n_y and n_z by $n_i^2 = \varepsilon_i / \varepsilon_o$, the equation (2.16) can be rewritten as:

$$\frac{x^2}{n_x^2} + \frac{y^2}{n_y^2} + \frac{z^2}{n_z^2} = 1 \quad (2.18)$$

The equation (2.18) is the equation of a general ellipsoid with major axes parallel to the x , y , and z directions whose respective lengths are $2n_x$, $2n_y$, and $2n_z$. This ellipsoid is known as the index ellipsoid and is used mainly to define the two indices of refraction and the two corresponding directions of D associated with the two independent plane waves that can propagate along an arbitrary direction in a crystal.

Furthermore, we define the impermeability tensor,

$$\eta_{ij} = (\varepsilon^{-1})_{ij} \quad (2.19)$$

where ε^{-1} is the inverse of the dielectric tensor ε and which form in the principal axis system of the crystal is:

$$\eta = \begin{pmatrix} \frac{1}{n_x^2} & 0 & 0 \\ 0 & \frac{1}{n_y^2} & 0 \\ 0 & 0 & \frac{1}{n_z^2} \end{pmatrix} \quad (2.20)$$

As a result, the equation of the index ellipsoid can be rewritten as:

$$r \cdot \eta \cdot r = 1 \quad (2.21)$$

Any plane through the origin of the index ellipsoid defines an intersecting ellipse as shown in Figure 20.

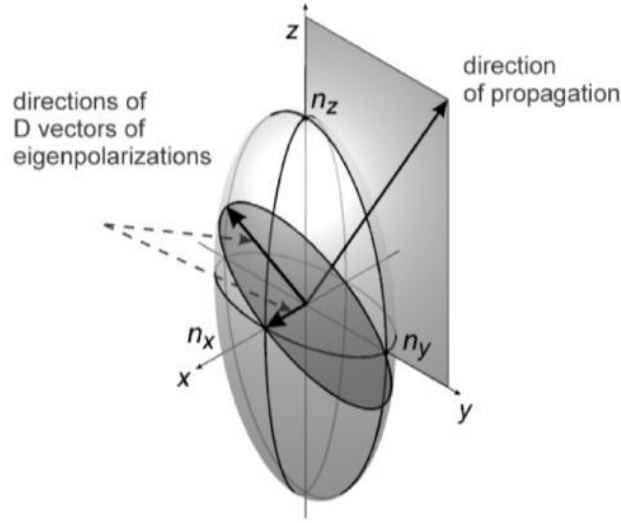


Figure 20: An intersection of the index ellipsoid with the plane normal to the direction of incidence \mathbf{d} of the electromagnetic wave.

In case where an external electric field is applied, changes the properties of an optically active crystal. The refractive index becomes a function of the external field, which has as result the change of the orientation and shape of the index ellipsoid. Especially for high electric fields, the polarization becomes nonlinear in electric field and can be described by the equation (1.3). Also, as we can see from the equations (2.10) and (2.19), the susceptibility tensor χ is related with the impermeability tensor η . This means that the impermeability tensor also contains terms of higher order in the presence of a strong external electric field and can thus be expanded using a Taylor-expansion around $E=0$:

$$\eta_{ij} = \eta_{ij}(0) + r_{ijk} E_k + s_{ijkl} E_k E_l + \dots \quad (2.22)$$

where E is the applied electric field and we neglect higher order terms in the Taylor expansion because they are too small for most applications. The constant r_{ijk} is the linear (or Pockels) electro-optic coefficient and s_{ijkl} is the quadratic (or Kerr) electro-optic coefficient. For gallium phosphide (GaP) and zinc telluride (ZnTe) which are commonly used in electro-optic sampling, their order of magnitude is:

$$r_{ijk} \approx 10^{-12} \frac{m}{V} \quad (2.23)$$

$$s_{ijkl} \approx 10^{-21} \frac{m^2}{V^2} \quad (2.24)$$

Thus, for ZnTe and GaP crystals, the Kerr effect can be neglected and then the equation (2.22) can be written as:

$$\eta_{ij} = \eta_{ij}(0) + r_{ijk} E_k \quad (2.25)$$

As the η is a symmetric tensor ($r_{ijk} = r_{jik}$), the tensor can be simplified by introducing the following:

$$\begin{aligned} r_{11k} &\rightarrow r_{1k} \\ r_{22k} &\rightarrow r_{2k} \\ r_{33k} &\rightarrow r_{3k} \\ r_{23k} = r_{32k} &\rightarrow r_{4k} \\ r_{13k} = r_{31k} &\rightarrow r_{5k} \\ r_{21k} = r_{12k} &\rightarrow r_{6k} \end{aligned} \quad (2.26)$$

So, the equation of the index ellipsoid in the presence of an external electric field can be written in terms of the relationship (2.21) as:

$$\begin{aligned} &\left(\frac{1}{n_x^2} + r_{1k} E_k \right) x^2 + \left(\frac{1}{n_y^2} + r_{2k} E_k \right) y^2 + \left(\frac{1}{n_z^2} + r_{3k} E_k \right) z^2 \\ &+ 2yzr_{4k} E_k + 2zxr_{5k} E_k + 2xyr_{6k} E_k = 1 \end{aligned} \quad (2.27)$$

where the indices 1, 2, 3 correspond to the principal axes x, y, z , and n_x, n_y, n_z are the principal refractive indices.

Crystals of the zinc blende structure such as ZnTe and GaP are composed of two face-centered cubic lattices shifted by one quarter of the spatial diagonal and thus feature a high degree of symmetry (cubic symmetry $\bar{4}3m$). Because of the high degree of symmetry, ZnTe and GaP crystals are optically isotropic at vanishing electric fields ($n_x = n_y = n_z = n_o$). In addition, the electro-optic tensor r_{ijk} has only one independent element ($r_{41} = r_{52} = r_{63} \neq 0$). The equation 2.19 can be written now as:

$$\frac{x^2}{n_x^2} + \frac{y^2}{n_y^2} + \frac{z^2}{n_z^2} + 2yzr_{41} E_x + 2zxr_{52} E_y + 2xyr_{63} E_z = 1 \quad (2.28)$$

or

$$\frac{x^2 + y^2 + z^2}{n_o^2} + 2yzr_{41}E_x + 2zxr_{41}E_y + 2xyr_{41}E_z = 1 \quad (2.29)$$

The crystals used in electro-optic experiments are cut in the (110) plane as it is shown in Figure 21 because it produces a brighter signal rather than another crystal cut [33].

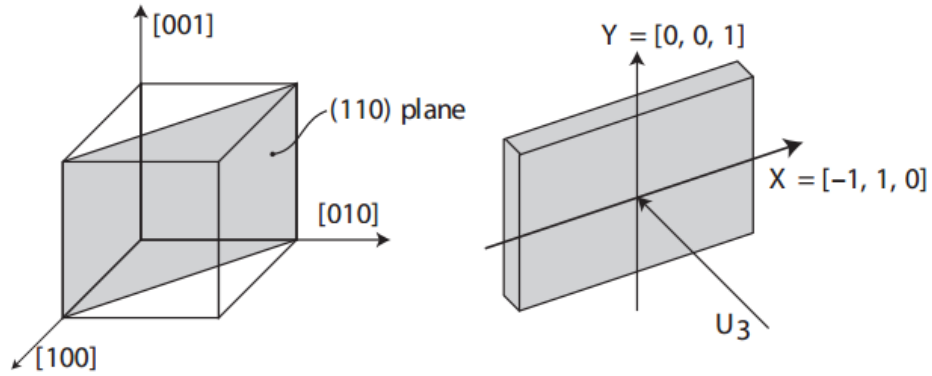


Figure 21: (Left) The (110) plane in which the used crystals are cut. (Right) The coordinate system (X, Y) [32].

A new coordinate system (X, Y) can be defined in this plane with:

$$X = \frac{1}{\sqrt{2}} \begin{pmatrix} -1 \\ 1 \\ 0 \end{pmatrix} \quad \text{and} \quad Y = \begin{pmatrix} 0 \\ 0 \\ 1 \end{pmatrix} \quad (2.30)$$

The THz radiation and the optical probe pulse incident perpendicular to this plane and are parallel to the vector U_3 , forming an angle θ with the X axis. Thus, the THz electric vector is written with respect to the new coordinate system as:

$$E_{THz} = E_{THz} \begin{pmatrix} -\frac{1}{\sqrt{2}} \cos a \\ \frac{1}{\sqrt{2}} \cos a \\ \sin a \end{pmatrix} \quad (2.31)$$

Inserting the previous equation into equation (2.25), we can find the principle axes (U_1 , U_2 , U_3) and the main refractive indices calculating the eigenvectors and the eigenvalues of the tensor η respectively [32]. From the eigenvalues, we have:

$$\begin{aligned} n_1 &= n_o + \frac{n_o^3 r_{41} E}{4} (\sin a + \sqrt{1 - 3 \cos^2 a}) \\ n_2 &= n_o + \frac{n_o^3 r_{41} E}{4} (\sin a - \sqrt{1 - 3 \cos^2 a}) \\ n_3 &= n_o - \frac{n_o^3 r_{41} E}{4} \sin a \end{aligned} \quad (2.32)$$

The refractive indices corresponding to the first two principal axes are n_1 and n_2 . The index ellipsoid is shown in the following Figure 22.

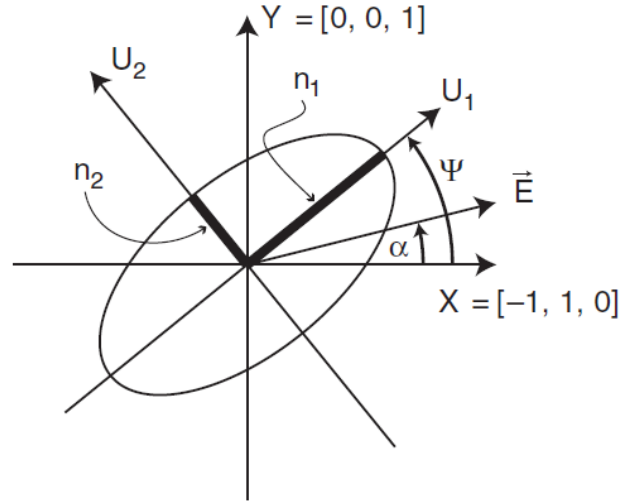


Figure 22: The refractive index ellipsoid projected into the (110) plane of the electro-optic crystal [32].

The optical beam is incident onto the electro-optic crystal along the normal to the (110) plane, its electric vector E_{laser} lies therefore in this plane. In the crystal the two components of E_{laser} along the principal axes U_1 and U_2 receive a relative phase delay:

$$\Gamma = \frac{2\pi d}{\lambda} \Delta n = \frac{2\pi d}{\lambda} (n_1 - n_2) = \frac{\pi n_o^3 d}{\lambda} r_{41} E \sqrt{1 + 3 \cos^2 a} \quad (2.33)$$

In order to measure this phase delay, we can use a balanced detection. In Figure 23 is represented the process of balanced measurement. A linearly polarized probe

beam is modified to elliptical polarization through the electro-optic process. A quarter-wave plate is used to bias the polarization of the probe beam. An analyzer (Wollaston prism) is used to split the biased probe beam into s and p polarization components and a pair of balanced photo-detectors is used to measure the difference between them. When no THz field is applied, s and p polarization components will have the same intensity after the analyzer and the balanced detector gives no signal. The presence of a THz electric field changes the polarization of the probe beam, generating a measurable signal in the balance detector which is:

$$S \propto \sin \Gamma \quad (2.34)$$

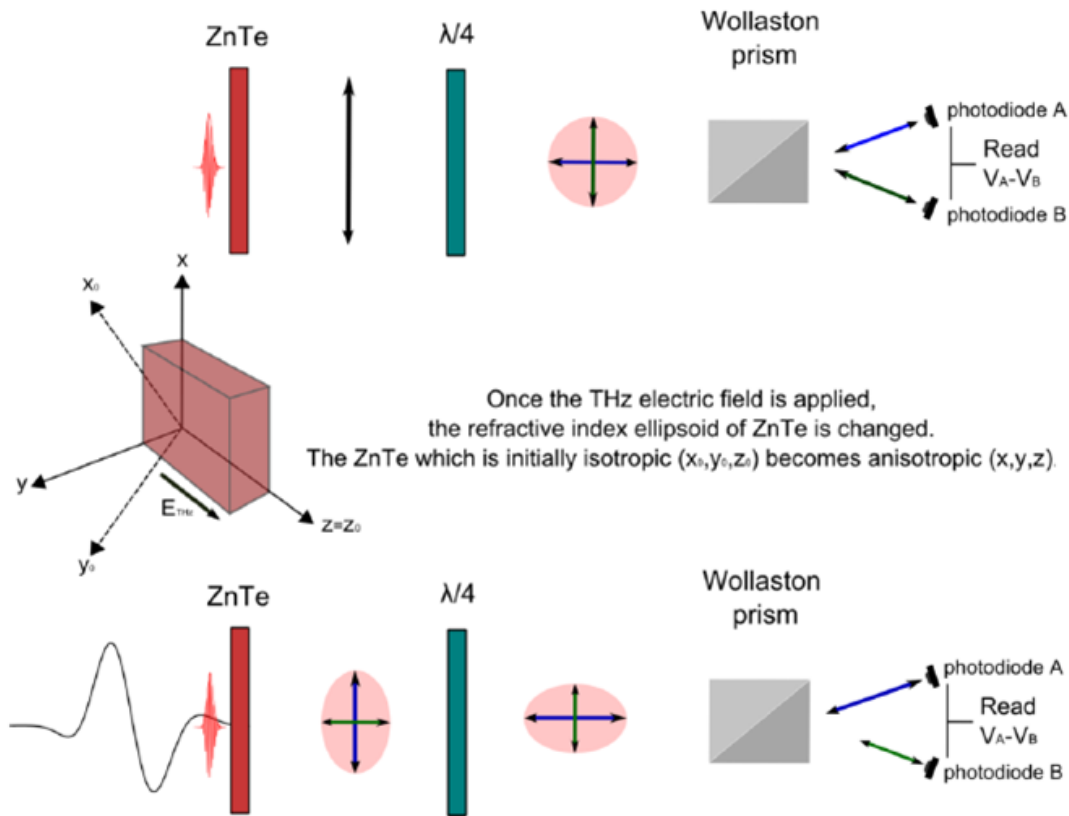


Figure 23: Schematic representation of a balanced electro-optic set-up.

The measurement of the THz electric field is performed by the aid of a lock-in amplifier. This device selectively amplifies the incoming signal in order to boost it above the noise level. To measure the entire THz waveform, a standard optical sampling is performed as follows. Owing to the periodicity of the laser pulses, we can use a pump probe method to measure the entire THz waveform. By changing the distance between the THz pulse and the optical probe pulse with an optical delay line, one can change the

time-delay between these two pulses and map the electric field of the THz pulse, $E(t)$, representing the temporal evolution of the pulse electric field. A schematic representation of the recorded THz signal at each different time delay is shown in Figure 24.

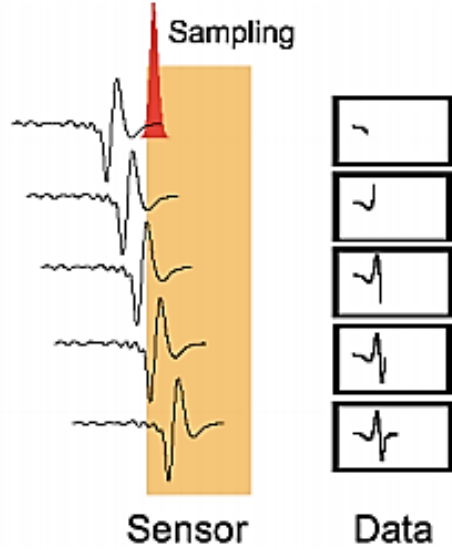


Figure 24: The measurement of the entire THz waveform.

2.4 Data analysis

By Fourier transforming the recorded temporal waveform of the THz pulse, $E(t)$, in the frequency domain, information about both amplitude and phase can be extracted:

$$E(\omega) = A(\omega)e^{-i\Phi(\omega)} = \int E(t)e^{-i\omega t} dt \quad (2.35)$$

The temporal evolution of the electric field of THz pulse is shown in Figure 25 (a) and Figure 25 (c) as function of the time delay of the probe pulse, using two of the most common e.o. crystals, a 500 μm thick ZnTe and a 100 μm thick GaP crystal respectively. After Fourier transform, the corresponding amplitude spectrum is obtained and is presented in Figure 25 (b) and Figure 25 (d). Two main factors limit the bandwidth of THz radiation in electro-optic sampling is the pulse duration of the excitation laser pulse and phase matching conditions. Roughly speaking, a laser pulse can generate a THz pulse with bandwidth twice that of the laser pulse bandwidth. Therefore, for laser pulse

duration of 35fs; the bandwidth is estimated to be above 60 THz. The limiting factor continues to be proper phase matching. Because the frequency extent of the THz pulses is so broad, it is practically impossible to select an e.o. material that fulfills phase matching requirements for all frequency components. For this reason, using the ZnTe crystal we can detect within a frequency range reaching up to 3 THz while with a GaP crystal the spectral bandwidth is expanding up to 8 THz.

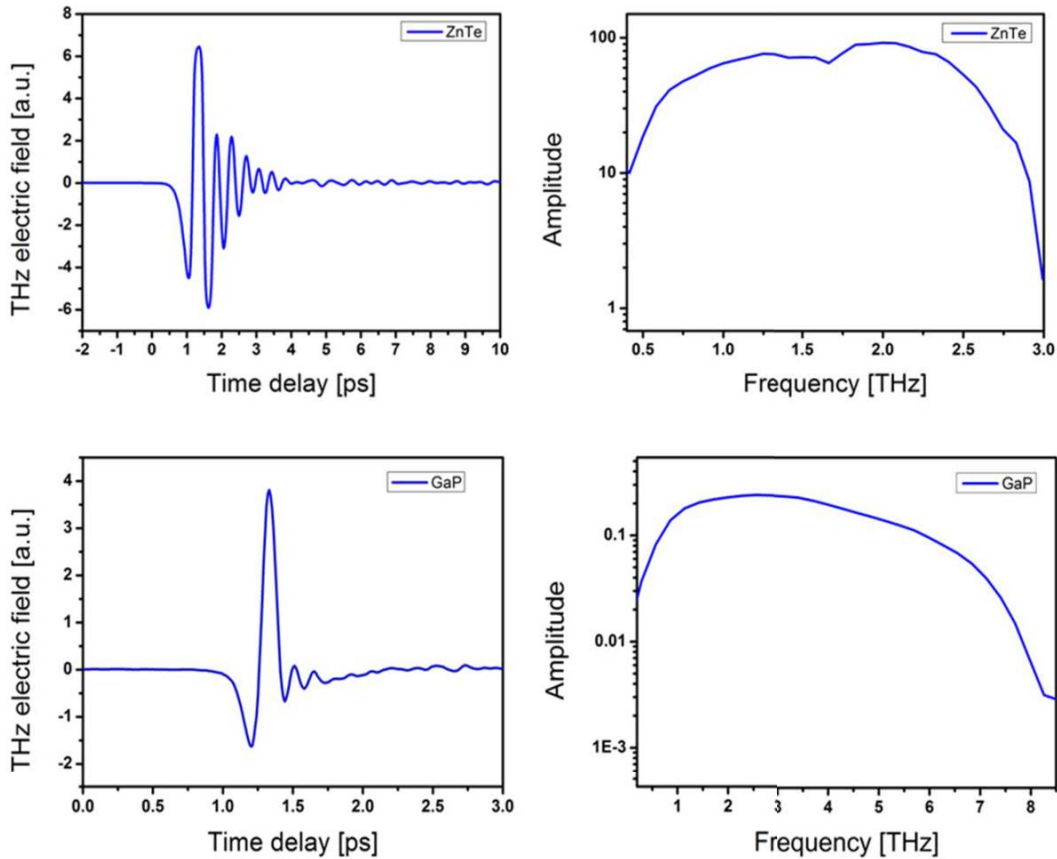


Figure 25: (a) Measured THz electric field with 0.5mm ZnTe crystal, (b) THz pulse spectral amplitude, (c) Measured THz electric field with 100µm GaP crystal and (d) its THz pulse spectral amplitude.

The frequency resolution is determined by the total scanning length l of the optical delay line. The frequency difference Δf between two neighboring points in the frequency spectrum is given by:

$$\Delta f = \frac{c}{2l} \quad (2.36)$$

where c is the speed of light. The resolution can in principle be improved by making l longer.

In a THz time-domain spectroscopic system (THz-TDS), the THz beam interacts with the sample and undergoes changes depending on the optical, chemical and structural properties of the sample are under investigation. In general there are three main physical effects to be taken into account in the measurement process; absorption, transmission and scattering. Absorption is the energy transfer from the THz wave to certain modes of the sample. In general, the intensity I of a light beam propagating through a material obeys the Beer-Lambert law:

$$I = I_o e^{-\alpha d} \quad (2.37)$$

where I_o is the intensity of the beam prior to propagation through a material of thickness d and absorption coefficient α .

The optical characterization of a material in the THz regime is accomplished by measuring the electric field $E_{sam}(t)$ of the transmitted THz pulse through the sample and normalizing it to a reference electric field $E_{ref}(t)$ without any sample (Figure 26).

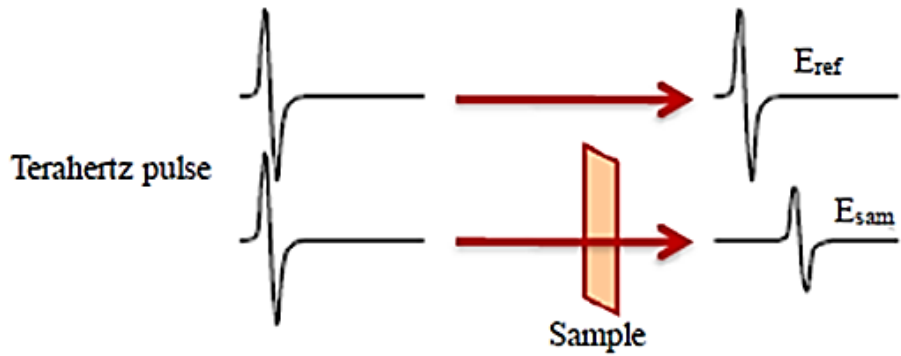


Figure 26: Representation of measuring the reference electric field and the sample electric field in transmission mode.

Taking the Fourier transform of the reference and sample electric field we can get the reference spectrum $A_{ref}(\omega)e^{-i\Phi_{ref}(\omega)}$ and the sample spectrum $A_{sam}(\omega)e^{-i\Phi_{sam}(\omega)}$. For a sample of known thickness d we can extract the following spectral properties such as its refractive index and absorption coefficient.

The refractive index can be expressed as:

$$n = 1 + \frac{[\Phi_{sam}(\omega) - \Phi_{ref}(\omega)]c}{\omega d} \quad (2.38)$$

where $\Phi_{sam}(\omega) - \Phi_{ref}(\omega)$ is the relative phase difference, c is the speed of light in vacuum, d is the sample thickness and ω is the radiation frequency.

The absorption coefficient is given by the following equation:

$$a = -\frac{2}{d} \ln \left(\frac{A_{sam}(\omega)}{A_{ref}(\omega)} \cdot T \right) \quad (2.39)$$

where d is the sample thickness, A_{sam} is the amplitude of the sample spectrum, A_{ref} is the amplitude of the reference spectrum and T is the Fresnel reflection coefficient for normal incidence and can be written as: $T = \frac{(n(\omega) + 1)^2}{4n(\omega)}$.

The absorbance $A(\omega)$ is derived by the following equation:

$$A(\omega) = -\ln \left(\frac{A_{sam}(\omega)}{A_{ref}(\omega)} \right) \quad (2.40)$$

From the refractive index, the complex permittivity can be calculated by:

$$\hat{\varepsilon} = \hat{n}^2 \quad (2.41)$$

where $\hat{n} = n + ik$ is the complex refractive index. In the complex refractive index k is the extinction coefficient, equal to: $k = \frac{\lambda a}{4\pi} = \frac{ca}{2\omega}$.

The real and imaginary part of the complex permittivity can be extracted and defined as:

$$\begin{aligned} \varepsilon' &= n^2 - k^2 \\ \varepsilon'' &= 2nk \end{aligned} \quad (2.42)$$

Four different samples were characterized optically in the THz regime using the GaP crystal in the detection of electro-optic sampling and using the aforementioned equations, their refractive index, absorption coefficient as well as the real and imaginary part of their complex permittivity has been defined. The studied samples were three

polymer samples: high density polyethylene (HDPE) with thickness 2.2 mm, Polytetrafluoroethylene (Teflon) with thickness 2.1 mm and Polymethylmethacrylate (PMMA) with thickness 1 mm and one 1 mm thick glass sample, Fused silica. The results are presented in Figure 27 and are in good agreement with previous reports [6, 34, 35].

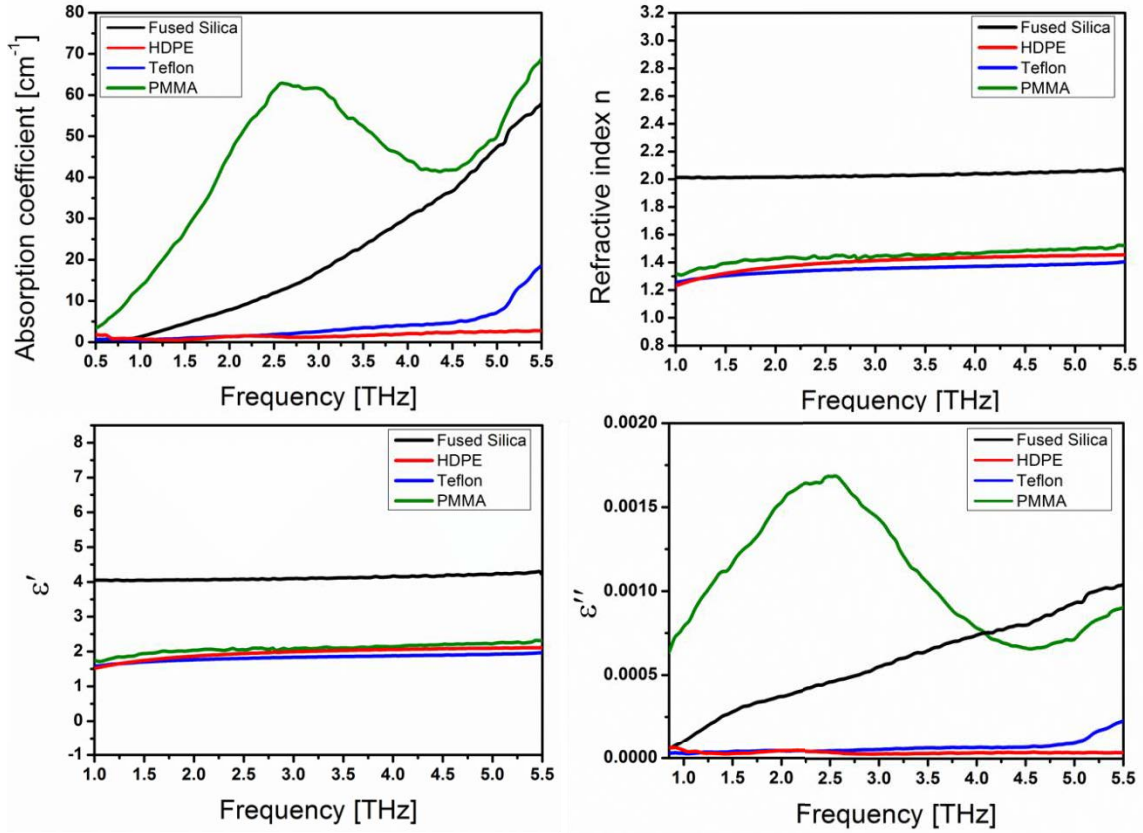


Figure 27: Calculated, (a) absorption coefficients, (b) refractive indexes, (c) real part of permittivity and (d) imaginary part of permittivity for different materials.

3. Terahertz spectroscopy of honey

3.1 THz spectroscopy in food industry

Food safety and quality concern have become more and more significant the last years. For this reason, there is an increasing interest on new, rapid and non-destructive techniques that can be applied to food quality evaluation or safety inspection, either to simplify, to speed up the checking process, or even to provide additional functionality. THz-TDS is a very promising technique for this purpose.

One of the attractive applications of THz-TDS in food quality control, exploiting the high absorbance of THz radiation by water, is the determination of moisture content in foods. This is an especially important application in controlling drying processes where low moisture content can alter the sensory qualities and shelf life of products. There is a number of studies where THz waves have been used to evaluate the moisture content of food such as wheat and food wafers [36, 37]. Also, the detection and characterization of water contamination of oils and other products is feasible using THz spectroscopy [38].

Another important role in the food industry plays the detection of foreign bodies in foods. THz radiation is not ionizing which is an advantage in contrast with other techniques like X-rays which aren't very safe for food screening. Unfortunately, most of the foods contain considerable amounts of water and, hence, cannot be penetrated by THz radiation. Nevertheless, THz systems may have some applications for quality control. For instance, it was early shown that chocolate is transparent to THz waves as it contains a small percentage of water and consists mostly of fat [39].

A lot of materials such as plastic, polymers, paper and glass are transparent materials to THz radiation. This makes THz spectroscopy and imaging attractive tools for quality validation of packaged products. Indeed, for the most applications, it is possible to carry out THz-TDS measurements while the materials are packaged [39].

Finally, the presence of pesticides or antibiotic residues in foods is of growing concern among consumers. Until now, a lot of screening methods and analyses are used for this purpose. Some of them are mass spectrometry and liquid chromatography which although are sensitive enough, they are time-consuming techniques and a pre-

treating of the sample is needed before the measurements [40, 41]. Near-infrared spectroscopy is only suitable for the quantitative analysis and not for qualitative analysis [42]. Infrared spectroscopy offers sharp features but is sensitive enough to the scattering phenomena. For this reason, it is more a quantitative tool rather than a qualitative one [43]. Nevertheless, traditional spectroscopic methods can only provide amplitude information. On the other hand, THz time domain spectroscopy provides information about the amplitude and the phase while it is rapid and non-destructive for the samples. However, quantitative detection of pesticides and antibiotics in the THz range is still at an initial stage [44, 45].

In this chapter we present the application of THz-TDS in food inspection. In particular, antibiotic residues and acaricides found in honey since they are often given to bees in order to fight against various diseases. Such chemicals can persist at trace levels in honey which is not a desired result. So far, THz spectroscopy and imaging have been applied to characterize optically bee's waxes and to measure the transmission of THz radiation through honey [46-48]. In this work, a number of different antibiotics and acaricides have been measured in the THz range between 0.3- 8 THz. Furthermore, studies have been performed in order to distinguish them in honey. An estimation of the concentration limits of these contaminants which can be detectable in honey using the THz-TDS technique is also given, aiming to use this novel technique in the production line. More details will be given in the following sections.

3.2 THz spectroscopy of honey: Qualitative and quantitative approach

3.2.1 Experiment and sample preparation

In this work, pellets of five different chemical substances have been made to classify their THz absorbance spectra. The chemical substances, purchased from Sigma-Aldrich are: amitraz (CAS 33089-61-1), coumaphos (CAS 56-72-4), tetracycline (CAS 60-54-8), sulfathiazole (CAS 72-14-0) and sulfapyridine (CAS 144-83-2). Among these five substances, the tetracycline, sulfapyridine and sulfathiazole are antibiotics and the amitraz and coumaphos are acaricides. All of these chemicals are commonly used during the production of honey.

The pellets were made with the use of High Density Polyethylene powder (HDPE) (CAS 9002-88-4) as a diluent material. The five substances were mixed with polyethylene powder in a concentration of 20% and then compressed into pellets with a hand

press. The thickness of the pellets was approximately 0.9 – 1.1 mm, their diameter was 7 mm and their total weight was around 40 mg. A pellet of pure HD-polyethylene was also made, as the reference sample.

The pellets are placed at the focus of the THz beam, by the aid of a sample holder consisted of two circular black Teflon plates of 5 mm clear aperture diameter (shown in Figure 28). All the measurements were taken at low levels of humidity (3.5-4.5 %) in order to avoid the absorption of THz radiation by the water vapor of normal air. Taking the Fourier transform of the recorded sample and reference electric fields and with the appropriate processing which was described in the previous chapter, we extracted their absorbance spectra.



Figure 28: (Left) The two plates where the pellet is deposited in between. (Right) Pictures of the sample holder being empty and with a pellet.

For performing measurements on honey and its mixture with antibiotics and acaricides, a different sample holder has been used. This holder consists of two circular plates of HDPE with a 2.54 cm diameter separated by a spacer of 620 μm thick, shown in Figure 29. The recorded spectra are normalized to the transmitted THz electric field through an empty sample holder and the level of humidity were all measurements have been done, was 1-2%.



Figure 29: Sample holder for honey and for the mixture of honey with antibiotics.

3.2.2 Results and discussion

In Figure 30, we present the absorbance spectra of the tetracycline, coumaphos, amitraz (left) and sulfapyridine, sulfathiazole (right) pellets in the THz region of 0.7 - 2.5 THz ($23.33 - 83.33 \text{ cm}^{-1}$). Coumaphos exhibits a distinct absorption peak at 1.88 THz (62.67 cm^{-1}), while we can't say the same for tetracycline and amitraz which do not exhibit any resonance peaks in this frequency range [45]. In Figure 30 (Right) are shown the absorbance spectra of the antibiotics sulfapyridine and sulfathiazole which belong to the sulphonamides family. Both of them show characteristic absorption peaks. In specific, sulfapyridine exhibits a resonance peak at 1.065 THz (35.66 cm^{-1}) which is in accordance with observations of previous reports [45] and sulfathiazole exhibits a number of absorption peaks with the most intense one observed at 2 THz ($66,66 \text{ cm}^{-1}$).

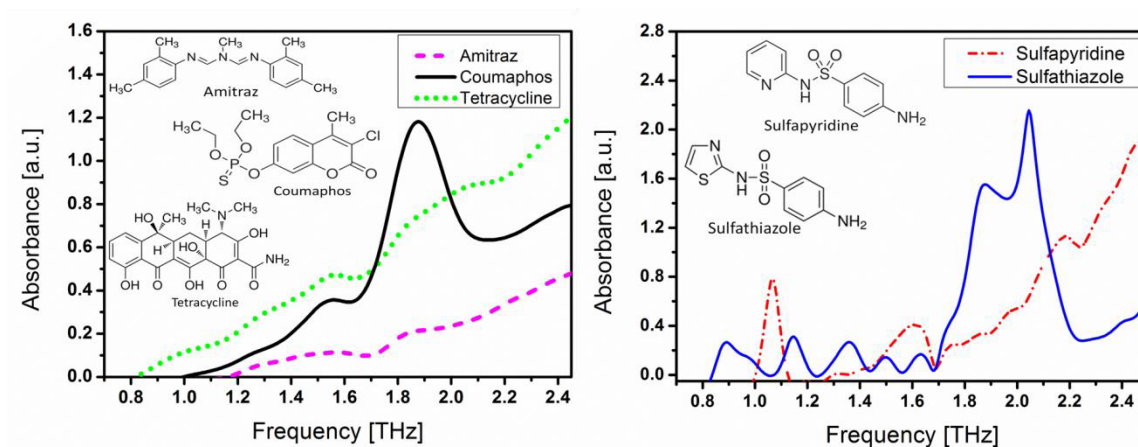


Figure 30: (Left) Absorbance spectra of tetracycline, coumaphos and amitraz in the frequency range between 0.7 THz and 2.5 THz. (Right) Absorbance spectra of sulfapyridine and sulfathiazole in the same frequency range. All of them are measured with ZnTe crystal and the measurements have been performed at room temperature and at low humidity levels (3.5-4.5) %

The frequency range where the spectra are recorded is limited not only from the ZnTe crystal which was used for the electro-optic detection, but also from interference phenomena coming from reflections of the THz pulses within the pellets that limit the lower useful end of the spectrum at frequencies above 0.7 THz. In order to provide information in a wider THz frequency range, a 100 μm thick GaP crystal has been used, expanding our detection limits up to 8 THz. Nonetheless, we couldn't manage to reach frequencies more than 5.6 THz due to the high absorbance of polyethylene and the studied chemical substances above this frequency. In Figure 31 are shown the absorbance spectra of all pellets as recorded using the GaP e.o. crystal.

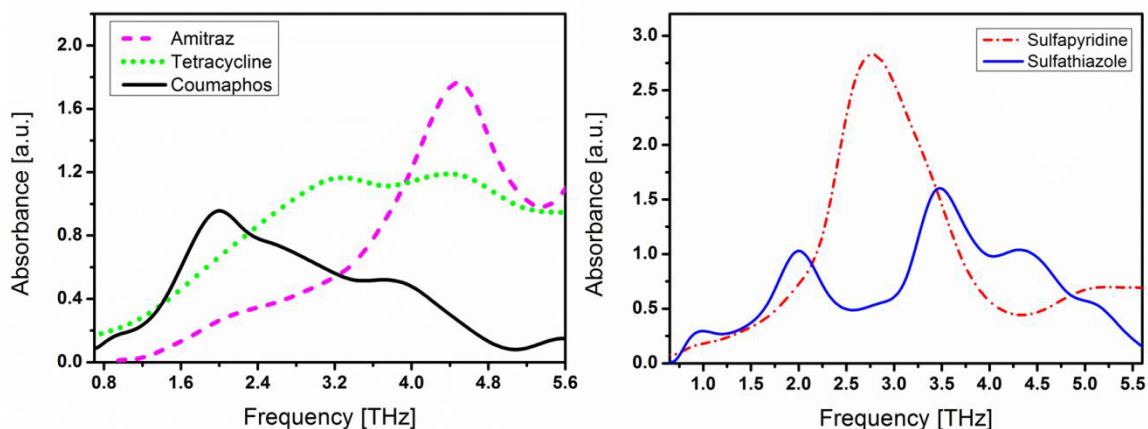


Figure 31: (Left) Absorbance spectra of tetracycline, coumaphos and amitraz in the frequency range between 0.7 THz and 5.6 THz. (Right) Absorbance spectra of sulfapyridine and sulfathiazole in the same frequency regime. All of them are measured with GaP crystal and the measurements have been performed at room temperature and at low humidity levels (3.5-4.5) %.

Similar to the previous measurements, coumaphos exhibits a strong absorbance peak around 1.9 THz which is broader and tetracycline doesn't exhibit any resonance peaks even at this extended THz region. On the other hand, for amitraz, a distinct resonance peak appears at 4.46 THz (148.7 cm^{-1}) as clearly shown in Figure 31 (Left-magenta). In Figure 31 (Right), are presented the absorbance spectra of the antibiotics sulfathiazole and sulfapyridine which show new characteristic spectral fingerprints in this frequency range.

Following the spectral analysis of these substances, we continued by mixing these chemicals with pure honey in order to verify if their presence in honey can be detectable. Initially, we recorded the THz transmission through pure honey which exhibits no distinct features (Figure 32), as expected.

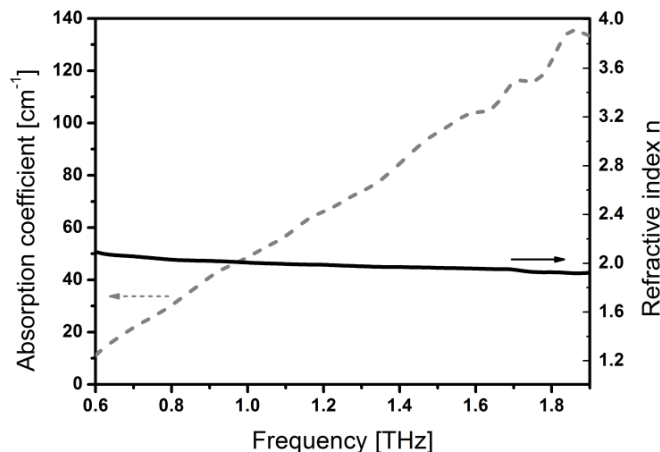


Figure 32: Optical properties (absorption coefficient and refractive index) of pure honey in the THz regime.

Having characterized optically the pure honey, we continued by mixing it with the antibiotics, sulfapyridine and sulfathiazole which show the strongest absorption peaks. The results of this mixture are presented in the next figures. In Figure 33 (Left) is shown the absorbance spectrum of the antibiotic sulfapyridine mixed with pure honey in a concentration of 10% (black line) in comparison to the pure sulfapyridine's spectrum (red line). As we observe, the distinct fingerprints of sulfapyridine are present but slightly shifted towards lower frequencies, although the antibiotic is mixed with honey. In Figure 33 (Right) we can see the absorbance spectrum of the antibiotic sulfathiazole when it is mixed with pure honey in a concentration of 12.5% (blue line) and again we can see that a number of resonance peaks are shifted in comparison to the resonances observed at the pellet (green line).

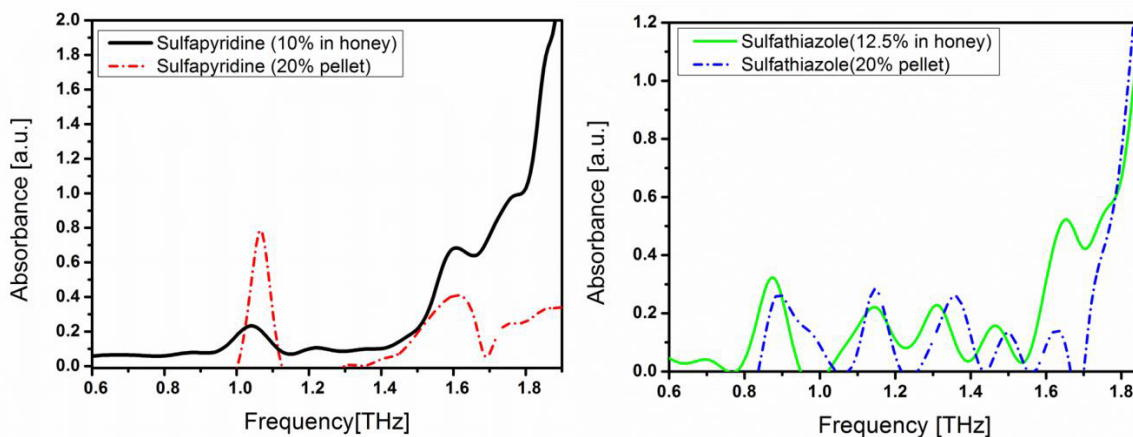


Figure 33: (Left) Absorbance spectrum of sulfapyridine mixed with pure honey in comparison with it in pellet. (Right) Absorbance spectrum of sulfapyridine mixed with pure honey in comparison with it in pellet.

It is obvious from the previous findings that we manage to distinguish both of these antibiotics when they are mixed with pure honey. Following these measurements, we continued by mixing both sulfapyridine and sulfathiazole, with pure honey in order to check if multiple substances can be distinguished in honey. The concentration for each one antibiotic is the same as previously (10% sulfapyridine and 12.5% sulfathiazole). In Figure 34 are shown the absorbance spectrum of sulfapyridine (black line), sulfathiazole (blue line) in comparison to the spectrum that is recorded when both of these antibiotics are mixed with honey (orange line). As it is clear, the resonance peaks of each one antibiotic are present in the mixture.

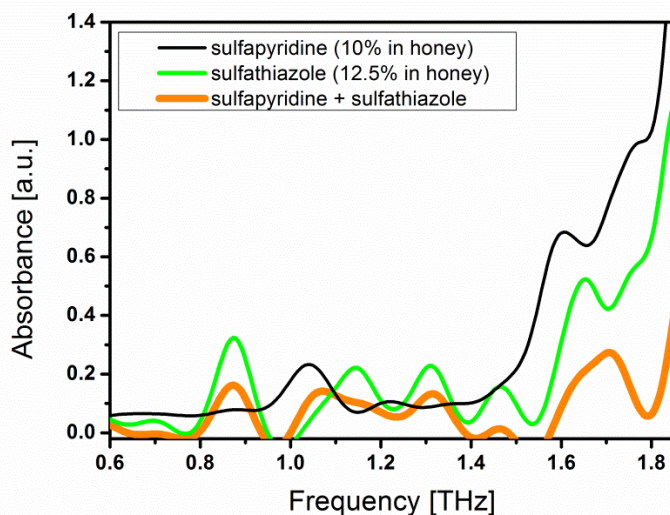


Figure 34: Absorbance spectra of sulfapyridine (black line), sulfathiazole (blue line) and the two of them mixed with honey.

In all measurements we observed that when the antibiotics are mixed with honey, their distinct resonance peaks are slightly shifted compared to the ones observed when they were studied as pellets. According to previous reports [49], it has been noticed that the form of a substance either it is anhydrous or hydrated influences its absorbance spectrum. This is attributed to the different intermolecular vibrational modes mediated by hydrogen-bonding in the presence of water or not. In our case, honey consists of approximately 20% water, so this explanation seems to be valid also for our studies. In order to verify this assumption, the sulfapyridine pellet was hydrated. In Figure 35 consecutive measurements of the hydrated pellet are presented, recorded at different times. When the sulfapyridine pellet is fully hydrated (black line) the resonance peak is shifted from 1.065 THz to 1.07 THz. After two more measurements at different times (magenta and green line), the resonance peak (blue line) is observed to be at the same position with the resonance peak of anhydrous sulfapyridine pellet (red

line) indicating that the shift of the resonance peaks, observed in the mixtures of the honey, can be attributed to the presence of water in the honey.

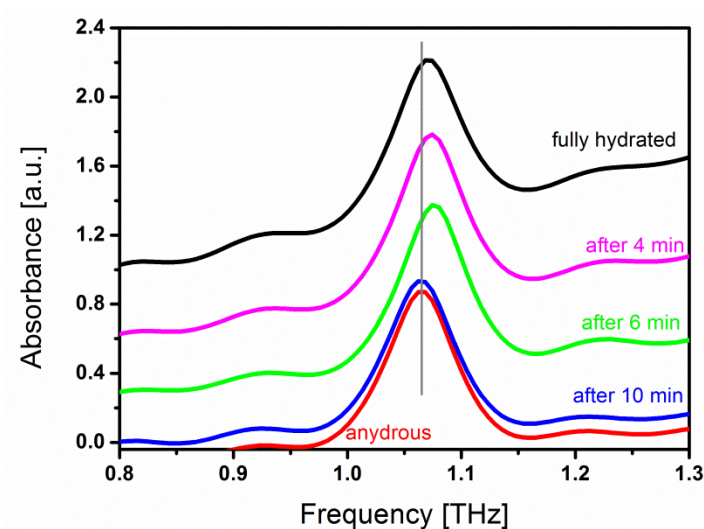


Figure 35: Consecutive measurements hydrated sulfapyridine pellet.

Furthermore, in order to give estimation for the concentration limit we can detect, we measured different concentrations of the antibiotic sulfapyridine mixed with pure honey reaching up to the minimum. In Figure 36 are illustrated the absorbance spectra of sulfapyridine in concentrations 13%, 11%, 5% and 2% respectively, zoomed in the frequency range where the strongest absorption peak was observed. As shown the resonance peak can be clearly seen in concentrations 13% and 11% while it is not obvious in concentrations 5% and 2%.

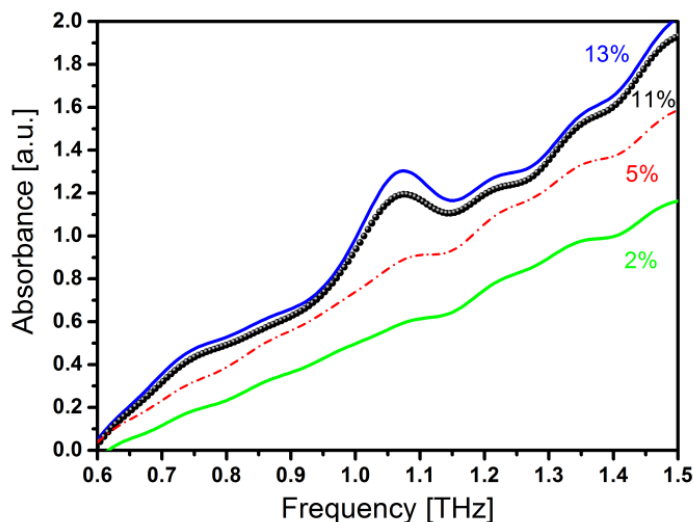


Figure 36: Absorbance spectrum of sulfapyridine mixed with pure honey in concentrations 13%, 11%, 5% and 2%.

Different mathematical ways of data processing were used in order to extract information from the recorded data. By taking the square root of the squared absorbance's first derivative we observe (Figure 37) that even at low concentrations the resonance peak of the antibiotic is present in the spectrum.

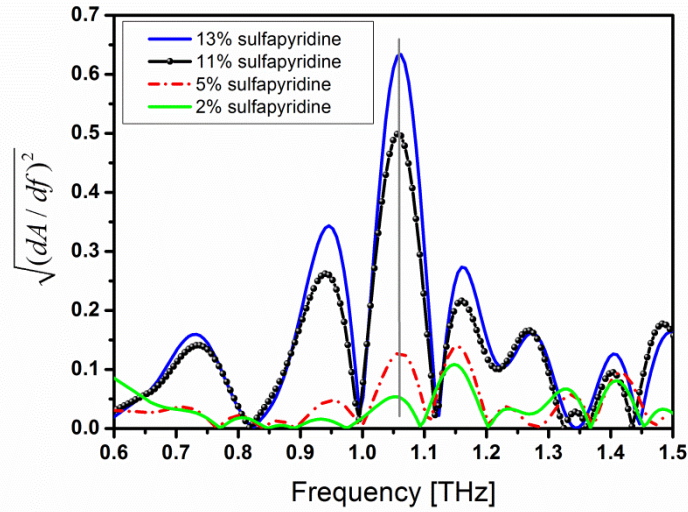


Figure 37: The square root of the squared absorbance's first derivative

Subsequently, by plotting the first derivative of the absorption peak as a function of the corresponding concentration is estimated that we can reach concentrations of an order of magnitude below of 2%, indicating that THz –TDS can be applied for the detection of small concentrations of antibiotics in honey (Figure 38).

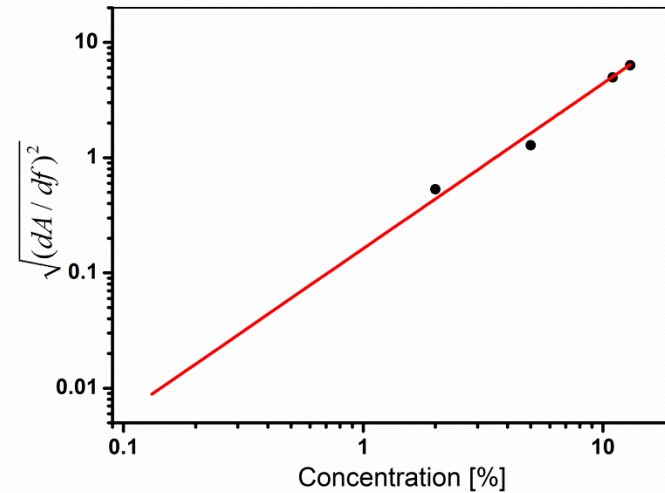


Figure 38: First derivative of the absorbance peak as a function of the corresponding concentration.

In conclusion, this work demonstrates that the THz-TDS system used in this study enables the novel application of THz spectroscopy for the detection of antibiotic and acaricides residues in honey. First of all, spectral features in the THz frequency range of different chemical substances which are used in honey production were presented. The THz absorbance spectra of a number of these substances are reported for first time in this work. Secondly, we presented the capability of THz spectroscopy to distinguish substances when they are mixed with pure honey. Finally, we tried to estimate the minimum concentration limit we can detect with our spectroscopic technique. This limit is far from the provided thresholds which mean that our analysis needs improvement. Nevertheless, THz-TDS can be used for a first check of the samples because it is a fast technique and it doesn't need a pre-treating of the sample. According to our results, THz spectroscopy seems to be a really promising and analytical tool in food inspection. Ultimate goal in the near future is the use of a mobile THz system for commercial use which can be used directly into the production line for honey and generally for food inspection.

4. Terahertz spectroscopy of pharmaceutical products

4.1 THz spectroscopy and pharmaceutical applications

Another research field, in which THz technology can be applied as a novel spectroscopic technique thanks to the unique properties of THz radiation, is the pharmaceutical industry. One of the major interests in pharmaceutical industry is the physical characterization of pharmaceutical materials. Since many chemical compounds show specific fingerprints in the THz range, THz spectroscopy can be used for this purpose. Most pharmaceuticals have to be administered at very low doses and thus, small quantities are required to formulate a drug in a proper pharmaceutical dosage. So far, there isn't any analytical technique which is able to monitor online the pharmaceutical formulation and production.

THz spectroscopy due to the sensitivity of THz waves to intermolecular vibrations could provide useful information on the substances constituting a drug and eventually to be used as an analytical technique for monitoring the production line of drugs. Furthermore, THz waves have longer wavelengths than visible and infrared waves resulting in little scattering. The little scattering nature, when combined with low absorption makes THz radiation an excellent spectroscopic tool. The photon energy of THz waves that interact with the pharmaceutical materials is low compared with other radiations, so the damage to the pharmaceutical samples is negligible.

Moreover, polymorphism and crystallinity changes are two issues that occupy a special position in the pharmaceutical industry. Polymorphism is a well-known phenomenon for many organic molecular crystals, where the same compound can crystallize in a number of different crystal structures. On the other side, crystallinity refers to the degree of structural order in a solid. Both of these phenomena may impact on pharmaceutical properties of a drug, for example, different polymorphs may have different rates of dissolution or bioavailability, and may even affect the stability of the drug. So far a number of reports are shown the use of THz spectroscopy in order to examine the previous phenomena [50, 51].

In this chapter we present a small part of the application of THz-TDS in pharmaceutical industry. In cooperation with a pharmaceutical industry, we have the chance to examine our spectroscopic technique in this field. The emphasis of work which is still in progress is based on a pharmaceutical tablet and its spectroscopic analysis with ultimate goal to see if can control the dosages of the excipients in the production line. The first step has been done already with the optical characterization of the tablet's excipients which gave very encouraging and promising results for the continuation of this research.

4.2 THz spectroscopy of pharmaceutical products: Qualitative and quantitative approach

4.2.1 Experiment and sample preparation

In this work, pellets of the pharmaceutical tablet's substances have been made to classify their THz absorbance spectra. These substances were: the active substance Diosmin, the excipients Microcrystalline Cellulose, Gelatine, Talc, Sodium starch glycolate and Magnesium stearate and a coating.

The pellets were made with the use of High Density Polyethylene (HDPE) powder as a diluent material due to its transparency to terahertz radiation. Each one of the substances was mixed with the polyethylene powder in a concentration of 20% and then compressed into pellets with the hand press. The thickness of the pellets was approximately 1–1.4 mm, their diameter was 7mm and their total weight was around 40 mg. A pellet of pure HD-polyethylene was also made, as the reference sample. The pellets were placed in the sample holder which was described in the previous chapter and is shown in Figure 39. Similar to the previous experiments described in this work, the pellets are placed at the focus of the THz beam and all measurements are taken at low levels of humidity (1-1.3 %).



Figure 39: Sample holder for pellets, being empty (left) and with a pellet (right).

4.2.2 Results and discussion

In Figure 40 we present the absorbance spectrum of Diosmin (left) and Microcrystalline cellulose (right) pellets in the THz region of 0.6 – 6 THz ($20 - 200 \text{ cm}^{-1}$) and 0.5 – 6.5 THz ($16.66 - 216.66 \text{ cm}^{-1}$) respectively. As it is clear from the absorbance spectrum of Diosmin, it exhibits a distinct absorption peak at 4.64 THz (154.66 cm^{-1}). Diosmin is an active constituent of many pharmaceutical tablets. As a result, until now there are a lot of reports about Diosmin and its determination in pharmaceutical drugs with different spectroscopic methods [52-55]. Nevertheless, in this research the absorbance spectrum of Diosmin in the THz frequency range was recorded for first time. On the other side, Microcrystalline Cellulose exhibits clearly two resonance peaks at 3.03 THz (101 cm^{-1}) and at 5.22 THz (174 cm^{-1}) which are in accordance with observations in other reports [56, 57].

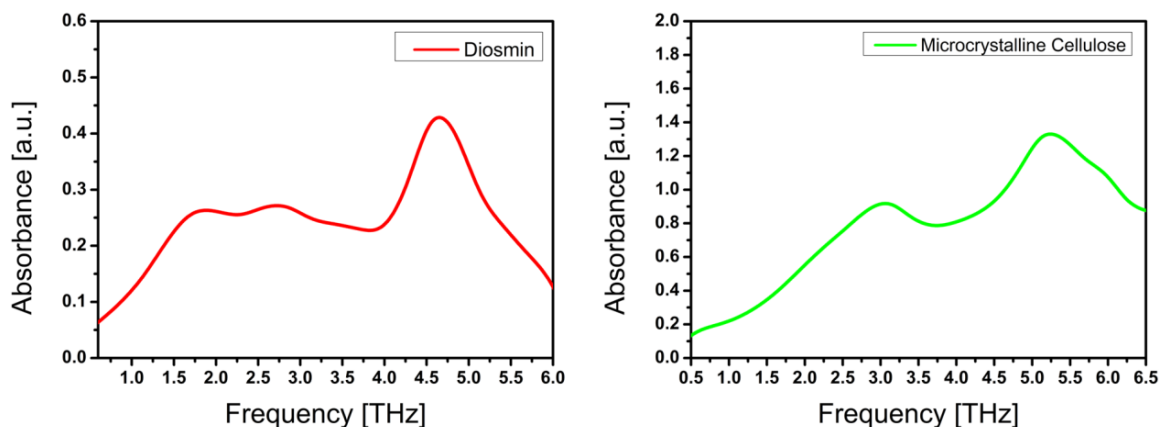


Figure 40: (Left) Absorbance spectrum of Diosmin in the frequency range between 0.6 THz and 6 THz. (Right) Absorbance spectrum of Microcrystalline Cellulose in the frequency range between 0.5 THz and 6.5 THz. All the measurements have been taken with GaP crystal in the detection.

In Figure 41 are shown the absorbance spectra of two more substances of the pharmaceutical tablet; Sodium starch glycollate and Gelatine which are also commonly used in pharmaceutical industry. Sodium starch glycollate, absorbs in the THz frequency range between 0.5 THz and 5.5 THz but it doesn't show any resonance peak in this frequency range. Gelatine exhibits a broad absorbance peak at 2.75 THz (91.66 cm^{-1}) [56].

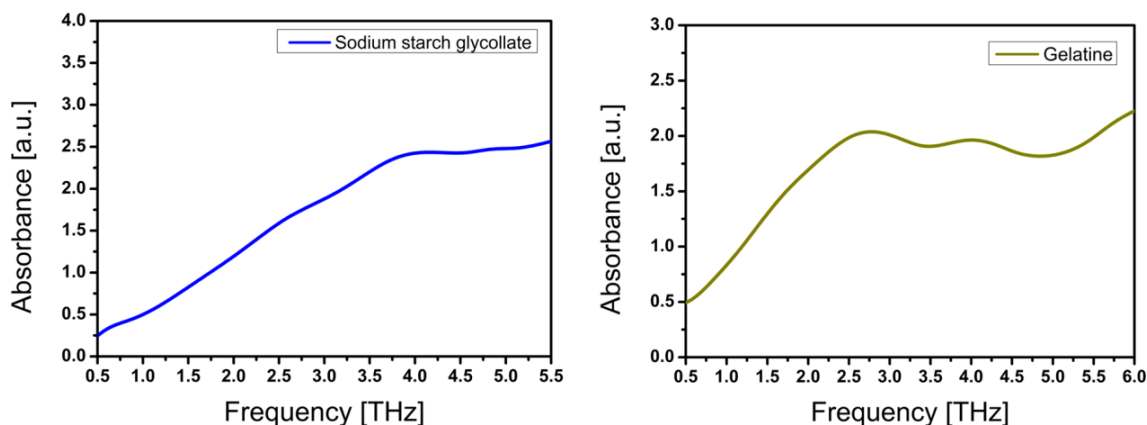


Figure 41: (Left) Absorbance spectrum of Sodium starch glycollate in the THz regime between 0.5 THz and 5.5 THz. (Right) Absorbance spectrum of Gelatine in the frequency range between 0.5 THz and 6 THz. All the measurements have been taken with GaP crystal in the detection.

In Figure 42 (Left) is shown the absorbance spectrum of Talc from 0.5 THz to 6.8 THz ($16.66 - 226.66 \text{ cm}^{-1}$) and in Figure 42 (Right) is shown the absorbance spectrum of Magnesium stearate from 0.6 THz to 5.5 THz ($20 - 183.33 \text{ cm}^{-1}$). Talc exhibits an absorption peak at 5.16 THz (172 cm^{-1}), but we can't say the same for Magnesium stearate. It seems not to absorb in this frequency range which is in accordance with previous reports [57].

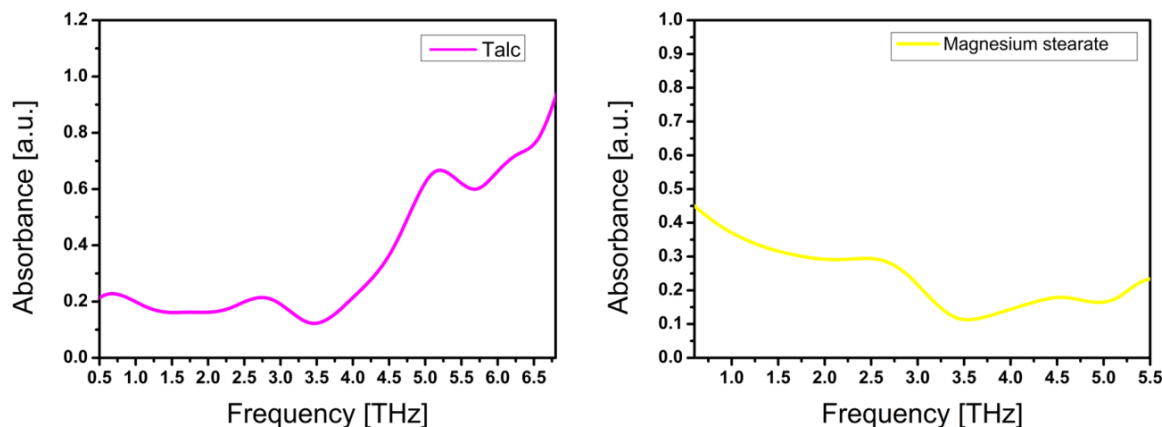


Figure 42: (Left) Absorbance spectrum of Talc in the frequency range between 0.5 THz and 6.8 THz. (Right) Absorbance spectrum of Magnesium stearate in the frequency range between 0.6 THz and 5.5 THz. All the measurements have been taken with GaP crystal in the detection.

The last excipient we measured was the coating of the pharmaceutical tablet and the result is represented in Figure 43. It is obvious from the figure that in the THz frequency range between 0.6 THz and 6 THz ($20 - 200 \text{ cm}^{-1}$), the coating exhibits a characteristic resonance peak at 3 THz (100 cm^{-1}).

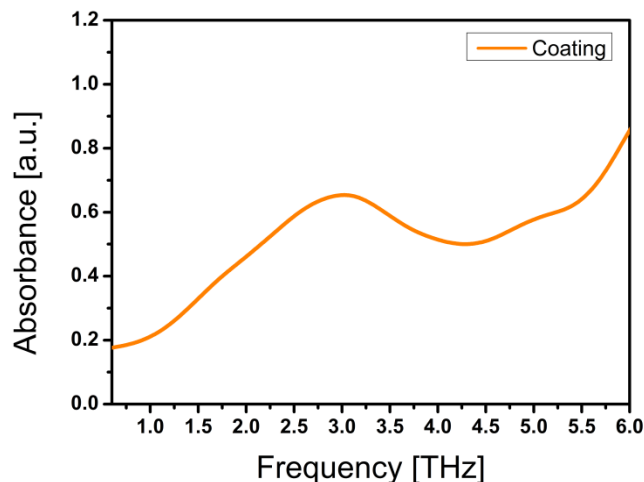


Figure 43: Absorbance spectrum of Coating in the THz regime between 0.6THz and 6THz.

In summary, this work which is in an initial stage demonstrates the potential of THz-TDS in pharmaceutical industry. So far we managed to characterize optically the active substance and the excipients of our pharmaceutical tablet in the THz frequency regime. Some of these results are in accordance with already published results and some of them are represented in this work for first time. An ultimate goal from our work is to examine the potential of THz-TDS to distinguish each one of the substances measuring the whole tablet and also the concentration limit which we can reach in order to check the dosages of the excipients. In any case the application of THz spectroscopy and also of THz imaging in the future, in the research field of pharmaceutical industry seems to be very promising.

References

1. H. Rubens, and E. F. Nichols, "Heat Rays Of Great Wave Length," *Physical Review (Series I)* **4**, 314-323 (1897).
2. J. W. Fleming, "High-Resolution Submillimeter-Wave Fourier-Transform Spectrometry of Gases," *Microwave Theory and Techniques, IEEE Transactions on* **22**, 1023-1025 (1974).
3. C. Fattinger, and D. Grischkowsky, "Terahertz beams," *Applied Physics Letters* **54**, 490-492 (1989).
4. A. G. Markelz, A. Roitberg, and E. J. Heilweil, "Pulsed terahertz spectroscopy of DNA, bovine serum albumin and collagen between 0.1 and 2.0 THz," *Chemical Physics Letters* **320**, 42-48 (2000).
5. E. P. J. Parrott, Y. Sun, and E. Pickwell-MacPherson, "Terahertz spectroscopy: Its future role in medical diagnoses," *Journal of Molecular Structure* **1006**, 66-76 (2011).
6. M. Naftaly, and R. E. Miles, "Terahertz Time-Domain Spectroscopy for Material Characterization," *Proceedings of the Ieee* **95**, 1658-1665 (2007).
7. L. Ozyuzer, A. E. Koshelev, C. Kurter, N. Gopalsami, Q. Li, M. Tachiki, K. Kadowaki, T. Yamamoto, H. Minami, H. Yamaguchi, T. Tachiki, K. E. Gray, W.-K. Kwok, and U. Welp, "Emission of Coherent THz Radiation from Superconductors," *Science* **318**, 1291-1293 (2007).
8. V. P. Wallace, A. J. Fitzgerald, S. Shankar, N. Flanagan, R. Pye, J. Cluff, and D. D. Arnone, "Terahertz pulsed imaging of basal cell carcinoma ex vivo and in vivo," *British Journal of Dermatology* **151**, 424-432 (2004).
9. R. M. Woodward, V. P. Wallace, D. D. Arnone, E. H. Linfield, and M. Pepper, "Terahertz Pulsed Imaging of Skin Cancer in the Time and Frequency Domain," *Journal of Biological Physics* **29**, 257-259 (2003).
10. A. J. Fitzgerald, V. P. Wallace, M. Jimenez-Linan, L. Bobrow, R. J. Pye, A. D. Purushotham, and D. D. Arnone, "Terahertz Pulsed Imaging of Human Breast Tumors1," *Radiology* **239**, 533-540 (2006).
11. Z. D. Taylor, R. S. Singh, D. B. Bennett, P. Tewari, C. P. Kealey, N. Bajwa, M. O. Culjat, A. Stojadinovic, L. Hua, J. P. Hubschman, E. R. Brown, and W. S. Grundfest, "THz Medical Imaging: in vivo Hydration Sensing," *Terahertz Science and Technology, IEEE Transactions on* **1**, 201-219 (2011).

12. L. Hai-Bo, Z. Hua, N. Karpowicz, C. Yunqing, and Z. Xi-Cheng, "Terahertz Spectroscopy and Imaging for Defense and Security Applications," *Proceedings of the IEEE* **95**, 1514-1527 (2007).
13. K. Kawase, Y. Ogawa, Y. Watanabe, and H. Inoue, "Non-destructive terahertz imaging of illicit drugs using spectral fingerprints," *Opt. Express* **11**, 2549-2554 (2003).
14. E. Abraham, A. Younus, J. C. Delagnes, and P. Mounaix, "Non-invasive investigation of art paintings by terahertz imaging," *Applied Physics A: Materials Science & Processing* **100**, 585-590 (2010).
15. A. J. L. Adam, P. C. M. Planken, S. Meloni, and J. Dik, "TeraHertz imaging of hidden paintlayers on canvas," *Opt. Express* **17**, 3407-3416 (2009).
16. K. Fukunaga, and M. Picollo, "Terahertz spectroscopy applied to the analysis of artists' materials," *Applied Physics A: Materials Science & Processing* **100**, 591-597 (2010).
17. K. Fukunaga, Y. Ogawa, S. i. Hayashi, and I. Hosako, "Terahertz spectroscopy for art conservation," *IEICE Electronics Express* **4**, 258-263 (2007).
18. J. M. Manceau, A. Nevin, C. Fotakis, and S. Tzortzakis, "Terahertz time domain spectroscopy for the analysis of cultural heritage related materials," *Applied Physics B- Lasers and Optics* **90**, 365-368 (2008).
19. J. A. Zeitler, P. F. Taday, D. A. Newnham, M. Pepper, K. C. Gordon, and T. Rades, "Terahertz pulsed spectroscopy and imaging in the pharmaceutical setting - a review," *Journal of Pharmacy and Pharmacology* **59**, 209-223 (2007).
20. V. P. Wallace, P. F. Taday, A. J. Fitzgerald, R. M. Woodward, J. Cluff, R. J. Pye, and D. D. Arnone, "Terahertz pulsed imaging and spectroscopy for biomedical and pharmaceutical applications," *Faraday Discussions* **126**, 255-263 (2004).
21. P. F. Taday, "Applications of terahertz spectroscopy to pharmaceutical sciences," *Philosophical Transactions of the Royal Society of London. Series A: Mathematical, Physical and Engineering Sciences* **362**, 351-364 (2004).
22. A. A. Gowen, C. O'Sullivan, and C. P. O'Donnell, "Terahertz time domain spectroscopy and imaging: Emerging techniques for food process monitoring and quality control," *Trends in Food Science & Technology* **25**, 40-46 (2012).
23. X.-C. a. J. X. Zhang, *Introduction to THz Wave Photonics* (2010).
24. J. T. Darrow, X. C. Zhang, and D. H. Auston, "Power scaling of large-aperture photoconducting antennas," *Applied Physics Letters* **58**, 25-27 (1991).

25. D. Jianming, L. Jingle, and Z. Xi-Cheng, "Terahertz Wave Air Photonics: Terahertz Wave Generation and Detection With Laser-Induced Gas Plasma," *Selected Topics in Quantum Electronics, IEEE Journal of* **17**, 183-190 (2011).
26. D. Dooley, "Sensitivity of broadband pyroelectric terahertz detectors continues to improve," *Laser Focus World* **46**, 49-53 (2010).
27. G. Gallot, and D. Grischkowsky, "Electro-optic detection of terahertz radiation," *J. Opt. Soc. Am. B* **16**, 1204-1212 (1999).
28. A. Couairon, and A. Mysyrowicz, "Femtosecond filamentation in transparent media," *Physics Reports-Review Section of Physics Letters* **441**, 47-189 (2007).
29. D. J. Cook, and R. M. Hochstrasser, "Intense terahertz pulses by four-wave rectification in air," *Opt. Lett.* **25**, 1210-1212 (2000).
30. X. Xie, J. Dai, and X. C. Zhang, "Coherent Control of THz Wave Generation in Ambient Air," *Physical Review Letters* **96**, 075005 (2006).
31. K.-Y. Kim, J. H. Glowina, A. J. Taylor, and G. Rodriguez, "Terahertz emission from ultrafast ionizing air in symmetry-broken laser fields," *Opt. Express* **15**, 4577-4584 (2007).
32. S. Casalbuoni, H. Schlarb, B. Schmidt, P. Schmüser, B. Steffen, and A. Winter, "Numerical studies on the electro-optic detection of femtosecond electron bunches," *Physical Review Special Topics - Accelerators and Beams* **11**, 072802 (2008).
33. Q. Chen, M. Tani, Z. Jiang, and X. C. Zhang, "Electro-optic transceivers for terahertz-wave applications," *J. Opt. Soc. Am. B* **18**, 823-831 (2001).
34. R. Piesiewicz, C. Jansen, S. Wietzke, D. Mittleman, M. Koch, and T. Kürner, "Properties of Building and Plastic Materials in the THz Range," *International Journal of Infrared and Millimeter Waves* **28**, 363-371 (2007).
35. Y. S. Jin, G. J. Kim, and S. G. Jeon, "Terahertz dielectric properties of polymers," *J. Korean Phys. Soc.* **49**, 513-517 (2006).
36. H. S. Chua, P. C. Upadhy, A. D. Haigh, J. Obradovic, A. A. P. Gibson, and E. H. Linfield, "Terahertz time-domain spectroscopy of wheat grain," in *Infrared and Millimeter Waves, 2004 and 12th International Conference on Terahertz Electronics, 2004. Conference Digest of the 2004 Joint 29th International Conference on*(2004), pp. 399-400.
37. H. S. Chua, J. Obradovic, A. D. Haigh, P. C. Upadhy, O. Hirsch, D. Crawley, A. A. P. Gibson, L. F. Gladden, and E. H. Linfield, "Terahertz time-domain spectroscopy of

crushed wheat grain," in *Microwave Symposium Digest, 2005 IEEE MTT-S International*(2005), p. 4 pp.

38. S. Gorenflo, U. Tauer, I. Hinkov, A. Lambrecht, R. Buchner, and H. Helm, "Dielectric properties of oil–water complexes using terahertz transmission spectroscopy," *Chemical Physics Letters* **421**, 494-498 (2006).

39. C. Jördens, and M. Koch, "Detection of foreign bodies in chocolate with pulsed terahertz spectroscopy," *Optical Engineering* **47**, 037003-037003 (2008).

40. S. Sivakesava, and J. Irudayaraj, "Detection of inverted beet sugar adulteration of honey by FTIR spectroscopy," *Journal of the science of food and agriculture* **81**, 683-690 (2001).

41. Y.-A. Hammel, R. Mohamed, E. Gremaud, M.-H. LeBreton, and P. A. Guy, "Multi-screening approach to monitor and quantify 42 antibiotic residues in honey by liquid chromatography–tandem mass spectrometry," *Journal of Chromatography A* **1177**, 58-76 (2008).

42. M. E. Auer, U. J. Griesser, and J. Sawatzki, "Qualitative and quantitative study of polymorphic forms in drug formulations by near infrared FT-Raman spectroscopy," *Journal of Molecular Structure* **661–662**, 307-317 (2003).

43. P. Y. Han, M. Tani, M. Usami, S. Kono, R. Kersting, and X. C. Zhang, "A direct comparison between terahertz time-domain spectroscopy and far-infrared Fourier transform spectroscopy," *Journal of Applied Physics* **89**, 2357-2359 (2001).

44. H. Yuefang, and Z. Hongjian, "Qualitative and Quantitative Detection of Pesticides With Terahertz Time-Domain Spectroscopy," *Microwave Theory and Techniques, IEEE Transactions on* **58**, 2064-2070 (2010).

45. A. Redo-Sanchez, G. Salvatella, R. Galceran, E. Roldos, J.-A. Garcia-Reguero, M. Castellari, and J. Tejada, "Assessment of terahertz spectroscopy to detect antibiotic residues in food and feed matrices," *Analyst* **136**, 1733-1738 (2011).

46. T. Lo, I. S. Gregory, C. Baker, P. F. Taday, W. R. Tribe, and M. C. Kemp, "The very far-infrared spectra of energetic materials and possible confusion materials using terahertz pulsed spectroscopy," *Vibrational Spectroscopy* **42**, 243-248 (2006).

47. T. Otsuji, Y. Tsuda, T. Komori, A. El Fatimy, and T. Suemitsu, "Terahertz plasmon-resonant microchip emitters and their possible sensing and spectroscopic applications," in *Sensors, 2009 IEEE*(2009), pp. 1991-1996.

48. P. Mounaix, A. Younus, J. C. Delagnes, E. Abraham, L. Canioni, and M. Fabre, "Spectroscopy and terahertz imaging for sigillography applications," *J. Eur. Opt. Soc.-Rapid Publ.* **6** (2011).
49. H.-B. Liu, Y. Chen, and X. C. Zhang, "Characterization of anhydrous and hydrated pharmaceutical materials with THz time-domain spectroscopy," *Journal of Pharmaceutical Sciences* **96**, 927-934 (2007).
50. P. F. Taday, I. V. Bradley, D. D. Arnone, and M. Pepper, "Using terahertz pulse spectroscopy to study the crystalline structure of a drug: A case study of the polymorphs of ranitidine hydrochloride," *Journal of Pharmaceutical Sciences* **92**, 831-838 (2003).
51. C. J. Strachan, T. Rades, D. A. Newnham, K. C. Gordon, M. Pepper, and P. F. Taday, "Using terahertz pulsed spectroscopy to study crystallinity of pharmaceutical materials," *Chemical Physics Letters* **390**, 20-24 (2004).
52. R. C. Garner, J. V. Garner, S. Gregory, M. Whattam, A. Calam, and D. Leong, "Comparison of the absorption of micronized (Daflon 500® mg) and nonmicronized 14C-diosmin tablets after oral administration to healthy volunteers by accelerator mass spectrometry and liquid scintillation counting," *Journal of Pharmaceutical Sciences* **91**, 32-40 (2002).
53. Z. Moldovan, and H. Y. Aboul-Enein, "A SENSITIVE SPECTROPHOTOMETRIC METHOD FOR DETERMINATION OF DIOSMIN USING SODIUM NITROPRUSSIDE AS A CHROMOGENIC REAGENT," *Instrumentation Science & Technology* **39**, 135-148 (2011).
54. A. A. Bunaciu, G. E. Udristioiu, L. L. Ruță, Ș. Fleschin, and H. Y. Aboul-Enein, "Determination of diosmin in pharmaceutical formulations using Fourier transform infrared spectrophotometry," *Saudi Pharmaceutical Journal* **17**, 303-306 (2009).
55. A. M. El-Shafae, and M. M. El-Domiaty, "Improved LC methods for the determination of diosmin and/or hesperidin in plant extracts and pharmaceutical formulations," *Journal of Pharmaceutical and Biomedical Analysis* **26**, 539-545 (2001).
56. H. Wu, E. J. Heilweil, A. S. Hussain, and M. A. Khan, "Process analytical technology (PAT): Effects of instrumental and compositional variables on terahertz spectral data quality to characterize pharmaceutical materials and tablets," *International Journal of Pharmaceutics* **343**, 148-158 (2007).
57. J. Hisazumi, T. Suzuki, H. Nakagami, and K. Terada, "Quantification of Pharmaceutical Polymorphs and Prediction of Dissolution Rate Using Theophylline Tablet by Terahertz Spectroscopy," *Chemical and Pharmaceutical Bulletin* **59**, 442-446 (2011).

